DEVELOPMENT OF GRATING-COUPLED III-V SEMICONDUCTOR
QUANTUM WELL INFRARED DETECTORS BASED ON ENLARGED
QUANTUM WELLS AND MINIBAND TRANSPORT

BY

LARRY SHOUSAN YU

A DISSERTATION PRESENTED TO THE GRADUATE SCHOOL
OF THE UNIVERSITY OF FLORIDA IN
PARTIAL FULFILLMENT OF THE REQUIREMENTS
FOR THE DEGREE OF DOCTOR OF PHILOSOPHY

UNIVERSITY OF FLORIDA

1992

ACKNOWLEDGEMENTS

TABLE OF CONTENTS

DEVELOPMENT OF GRATING-COUPLED III-V SEMICONDUCTOR
QUANTUM WELL INFRARED DETECTORS BASED ON ENLARGED
QUANTUM WELLS AND MINIBAND TRANSPORT

By

LARRY SHOUSAN YU

August 1992

Chairman: Sheng S. Li
Major Department: Electrical Engineering

This work deals with the development of surface illumination long wavelength quantum well infrared photodetectors (QWIPs) by using planar metal grating couplers, enlarged quantum wells, and superlattice barrier miniband transport technique.

The first bound-to-miniband (BTM) transition GaAs/AlGaAs quantum well superlattice infrared photodetector is developed. The intersubband transition scheme is from the localized bound ground state in the enlarged quantum wells to the 'global' miniband of the superlattice (SL) barriers. By using resonant tunneling and coherent transport along the superlattice miniband, a high performance long wavelength infrared (LWIR) photodetector is demonstrated.

Similar work has also extended to the InP lattice-matched InAlAs/InGaAs system. A large enhancement of integrated infrared absorption strength was observed in a miniband reinforced quantum well/superlattice structure.

To further reduce the device dark current, a lightly strained step-bound-to-miniband (SBTM) transition InGaAs/GaAs/AlGaAs QWIP is demonstrated. A new

potential 'step' is incorporated into the superlattice barrier to block the undesirable electron tunneling current from the heavily doped ground state of the enlarged quantum well. A significant reduction in device dark current is achieved.

In order to facilitate large area surface illumination, a planar metal grating coupler is proposed and developed for both front normal and backside light incidence. A detailed study of the dependence of coupling efficiency on the grating periodicity of grating-coupled GaAs/AlGaAs quantum well infrared detectors has been performed.

Finally, a novel type-II quantum well infrared photodetector is demonstrated by utilizing an indirect $AlAs/Al_{0.5}Ga_{0.5}As$ system grown on [110] oriented GaAs substrate. The mechanisms of *normal incidence* and multiple spectral response property are discussed.

CHAPTER 1
INTRODUCTION

In recent years, there has been a lot of interest [1-8] in resonant tunneling and perpendicular quantum transport in superlattices, in large part motivated by the impressive progress achieved by molecular beam epitaxy (MBE) technique. The large electric dipole matrix element [9] existing between the subbands of the quantum well makes such a structure extremely attractive for long wavelength infrared detection [10-20], especially, in the atmospheric spectral range of $8-14\mu m$.

Heterojunction superlattices and their transport properties were first investigated by Esaki and Tsu in 1970 [1]. Due to the coupling effect between the wells, it was theoretically predicted by Kazarinov and Suris [2], in 1971, that the existence of $I - V$ (current-voltage) peaks is a negative differential conductance characteristic of superlattice corresponds to the resonant tunneling (RT) between the different states of adjacent wells. In 1973, Tsu and Esaki [21] computed the resonant transmission coefficient T^*T for double, triple, and quintuple barrier structures from the tunneling point of view. The oscillatory conductance along the superlattice axis in an AlAs/GaAs system was observed in 1974 [4]. The voltage period of the oscillations was comparable to the energy separation between the first two conduction minibands. In 1985, Capasso et al. demonstrated a novel effective mass filtering phenomenon [5] by using superlattice miniband transport. A new quantum conductivity and giant quantum amplification of photocurrent in a semiconductor superlattice was obtained.

The materials in which these devices are implemented are sufficiently advanced that there exists the possibility of incorporating these devices in high performance integrated circuits. One important application of the quantum well technology in-

volves infrared detection and image sensing. Work in this area has proceeded to the point where new types of infrared detectors and arrays based on quantum well structures are now feasible. In addition, further refinements of such detectors appear possible. A distinguishing feature of these infrared detectors is that they can be implemented in chemically stable wide bandgap materials, as a result of intersubband processes. Therefore, it is possible to use III-V material systems that have fewer processing problems than mercury cadmium telluride (MgCdTe), and to achieve monolithic integration in which both detector and signal processing circuits could also be implemented. In addition, flexibility associated with control over composition during epitaxial growth can be used to tailor the spectral response of quantum well infrared detectors to particular infrared bands or multiple bands. Quantum well detectors with response at various wavelengths from 0.5 to 20 μm have been demonstrated. Many infrared applications are possible including space surveillance. The uniformity of epitaxial growth over large areas could open the way to large arrays. In many respects, recent experimental work has borne out potential advantages of this approach. Effective means of modeling have been developed. Recent work has also dealt with improved means of coupling infrared radiation to electrons in quantum wells.

Modern molecular beam epitaxy (MBE) and metallorganic chemical vapor deposition (MOCVD) epitaxial growth techniques provide the ability to control and vary composition at the level of successive atomic layers during epitaxial deposition. Spatially modulated doping in conjunction with this control of the host alloy composition demonstrates very flexible and powerful means of device fabrication. A major portion of the studies up to now have been carried out with the GaAs/AlGaAs system. However, a variety of other systems, notably InGaAs/InAlAs, InAs/GaSb, InP lattice-matched alloys, strain-layer InGaAs/GaAs, SiGe/Si, are also under the investigation. Semiconductor hetero-interface exhibits the abrupt discontinuity in the local band structure, usually associated with a gradual band bending in its neigh-

borhood which reflects space-charge. Hetero-interfaces may be classified into four kinds: type I, type II staggered, type II misaligned, and type III. The conduction band discontinuity ΔE_c is equal to the difference in the electron affinities of the two semiconductors. Type I is a commonly used quantum well structures, which are applied to the GaAs/AlGaAs, GaSb/AlSb, GaAs/GaP systems. Particularly, type II is the quantum structure where electrons and holes are confined in the different semiconductor layers at their heterojunctions and superlattices. Type III is another interesting member of the family which has a zero energy bandgap, however, most of our experimental work and theoretical calculations described here are focused on type I, with some exploring effort focused on indirect type II quantum well structures.

The incorporation of superlattice and quantum well technology makes it possible to design and construct various novel quantum devices which are impossible to make previously. Several long wavelength infrared (LWIR) detectors based on miniband-to-miniband [6,7], bound-to-bound [10,11], bound-to-virtual excited state [12], and bound-to-continuum [13,14] state transition in the multiple quantum well structures have been extensively explored.

This dissertation focuses on a new class of long wavelength infrared (LWIR) detectors using the enlarged quantum well and short-period superlattice (SL) barrier structures. The infrared detection mechanism is based on the bound-to-miniband (BTM) transition and superlattice miniband transport. The normal illumination is realized by applying a planar metal grating contact onto the top of device. The major breakthrough and contributions made in this work are as follows:

(1) Demonstrated the first bound-to-miniband (BTM) transition and miniband transport GaAs/AlGaAs quantum well infrared detector.

(2) Observed a large enhancement of intersubband infrared absorption in a miniband reinforced bound-to-miniband transition InAlAs/InGaAs quantum well superlattice structure.

(3) Developed an ultra-low dark current step-bound-to-miniband (SBTM) transition QWIP by incorporating a new potential 'step' into the superlattice barrier to block the undesirable electron tunneling current from the heavily doped ground state.

(4) Developed a novel metal-grating coupler for both front normal and backside illumination. Significant improvements in large area detector quality, cost, and uniformity were achieved.

(5) Conducted a detailed study of coupling efficiency versus grating periodicity. One order of magnitude enhancement in device quantum efficiency η was obtained under normal illumination.

(6) Developed the first type-II quantum well infrared detector by using indirect AlAs/AlGaAs system on GaAs substrate grown along [110] direction. A desirable normal incidence and interesting multi-color photoresponse properties were achieved.

In Chapter 2, we introduce the use of superlattice barriers, which can be a replacement of equivalent bulk barriers with the same effective barrier potential height. Also, a variety of quantum well/superlattice selectivities and their advantages are addressed. Then, the minibands and their properties associated with the superlattice structure are reviewed.

Chapter 3 provides the basic and powerful mathematical tool to model and design the superlattice and multiple quantum well structures used for our study. It has numerous advantages over the conventional envelop wave function approximation method. It presents to us a relative simple and straightforward technique to solve what were previously considered to be complicated coupling effects, higher order energy states, carrier lifetimes, formation of miniband, and transmission coefficient of quantum well/superlattice structures. Chapters 4 and 5 describe the intersubband

absorption and dark current properties in a quantum well detector, and the relevant figures of merit for photoconductive detectors.

In Chapters 5 and 6, we present the novel bound-to-miniband (BTM) transition quantum well infrared detector based on wide quantum wells and short-period superlattice barriers. Detailed work and discussions are given for both a GaAs substrate lattice-matched GaAs/AlGaAs system and an InP substrate lattice-matched InAlAs/InGaAs system.

In Chapter 7, a new stepped potential ΔE_{STEP} is introduced into the superlattice barrier to form a step-bound-to-miniband (SBTM) transition QWIP. Unlike the previous devices, the new quantum wells use lightly strained InGaAs material and the barriers use the lattice-matched GaAs/AlGaAs superlattices. The mechanism of device dark current reduction is discussed.

The innovative large area normal incidence metal-grating couplers are fully depicted in Chapter 8. Both theoretical and experimental study of grating coupler optimization is presented in this chapter.

Chapter 9 presents our latest effort in exploring a new type-II AlAs/AlGaAs quantum well infrared detector. A normal incidence is achieved due to the tilted ellipsoidal energy band of the indirect III-V semiconductor material. By using the cross-interface transition, a desirable multi-color detector can be expected. Chapter 10 gives the summary and conclusions reached from this work.

CHAPTER 2
TWO-DIMENSIONAL SEMICONDUCTOR QUANTUM WELL AND SUPERLATTICE STRUCTURES

2.1 <u>Introduction</u>

With the advance of Molecular Beam Epitaxial (MBE) and Organometallic Chemical Vapor Deposition (OMCVD) techniques, high quality III-V semiconductor single crystal epitaxial layers are grown routinely with different doping concentrations and alloy compositions.

The discussion of an infinite one dimensional quantum well is often used as a simple example in introductory quantum physics. This elementary example takes on a particularly important realization with the advent of the ability to grow epitaxial layers with a thickness of nanometers, giving very significant quantized energy differences. The best quality quantum wells were grown on alternate layers of GaAs for the well and $Al_xGa_{1-x}As$ ($0 \leq x \leq 1$) for the barrier to the electrons. The confinement of the electrons occurs because the bandgap of $Al_xGa_{1-x}As$ ($E_g = 1.424 + 1.247\ x$ (eV) for x less than 0.45) is much larger than that of GaAs. Above this concentration of aluminum, the bandgap becomes indirect and the above formula is invalid. The AlGaAs/GaAs heterojunction system creates 65% of the bandgap difference in the conduction band potential, and a 35% difference in the valence band potential. Thus, the potential barrier height between the GaAs and the AlGaAs for the conduction band electrons is given by $\Delta E_c = 0.81\ x$ (eV), where x is the aluminum mole fraction.

The heterojunction interface in the GaAs/AlGaAs system usually is very smooth, with fluctuation in the well thickness typically less than 0.3 nm. The smoothness of the surface results from the thermodynamics of epitaxial layer growth in this lattice-

6

matched system. During the epitaxial layer growth, the deposited atoms of gallium, aluminum, or arsenic are given a thermal energy low enough to allow a high probability of remaining bound to the surface. However, this thermal energy is sufficiently high to permit the atoms to move around the surface. When an atom encounters a lattice site discontinuity with the planar surface, the binding energy of the atom increases since the atom is now bound on more than one side. If the increase in binding energy is sufficient, the atom has a strong preference to bind to the irregularities, and hence smoothing the surface. If the growth rate is held sufficiently low, then the growth occurs on a previously established irregularity. Thus after smoothing all the initial irregularities, the growth completes one atomic plane (about 2.8 $\mathring{A}$ for GaAs atomic pair in the [100] plane) before initiating a new atomic plane of growth. In a clean growth chamber, the fractional area of these imperfections is usually less than 0.01%. In general, two materials with different lattice constants will create lattice mismatch at the heterojunction interface with dislocations, resulting in poor heterointerface. Fortunately, GaAs and AlAs have very similar lattice spacings (5.642 $\mathring{A}$ and 5.661 $\mathring{A}$ respectively), with only a 0.34% lattice mismatch. This mismatch is even less for experimental conditions to be described, with only 40% of the gallium atoms substituting for the aluminum atoms in the $Al_xGa_{1-x}As$ barrier regions. A special advantage of the $Al_xGa_{1-x}As/GaAs$ system is that this good lattice match can be achieved by substituting only one atomic site, whereas more generally this match can be obtained only with the use of quaternary compounds. This advantage greatly eases the growth of this material system. The growth of high quality quantum wells is assisted by the isoelectronic nature of the Al and Ga atoms which lie in the same column of the periodic table in adjacent rows. Quantum well structures formed on a III-V material system have been shown to operate in devices at elevated temperatures for tens and thousands of hours with little degradation.

2.2 Intersubband Absorption

Quantum confinement of carriers in a semiconductor quantum well leads to the formation of discrete energy levels and the drastic change of optical absorption spectra. One of the most remarkable properties of this quasi-two-dimensional electronic system is that the optical transitions between the size-quantized subbands are feasible. Intersubband absorption corresponding to transitions between the first and the second electronic subband has recently been studied in n-type AlGaAs/GaAs multiple quantum well superlattices. The large dipole moment between the ground state and the higher subbands in doped semiconductor quantum wells (QWs) suggests the possibility of various long wavelength infrared (LWIR) detectors and modulators.

The eigen energy levels of a quasi-two-dimensional system can be calculated within the framework of effective mass approximation, provided that the complications associated with valley degeneracy, effective mass anisotropy, and the complex valence band structure of most III-V and group IV semiconductors are neglected. We have assumed that the electron effective mass m^* is derived from a single conduction band minimum. The one-electron wave function can be written as a product

$$\Psi(x, y, z) = u(\mathbf{r})\psi_n(z)exp(i\mathbf{k}_\perp \cdot \mathbf{r}) \tag{2.1}$$

where $\psi_n(z)$ is the envelope wave function for the nth subband, $u(\mathbf{r})$ is the periodic Bloch function associated with the bottom of the conduction band; $\mathbf{k}_\perp$ and $\mathbf{r}$ are vectors in two-dimensional wave-vector and configuration space, respectively.

Within the frame work of effective mass approximation, the Schrödinger equation for the envelope function is

$$\frac{d^2\psi_n}{dz^2} + \frac{2m}{\hbar^2}[E_n - V(z)]\psi = 0 \tag{2.2}$$

where m is the mass, E_n and ψ_n represent the energy eigenvalues and eigenfunctions of the bound state, respectively. V(z) is the potential function.

For an infinite quantum well, the electron wave functions and energy eigenvalues are given by

$$\varphi_n = A_n Sin(nk_n z)exp(i\mathbf{k}_t \cdot \mathbf{r}_t), \tag{2.3}$$

and

$$E = E_{z,n} + \frac{\hbar^2 k_x^2}{2m_x} + \frac{\hbar^2 k_y^2}{2m_y}, \tag{2.4}$$

Here we assume that one electron confinement is along the growth direction (i.e. z-direction). The intersubband transition oscillator strength f_{os} and the dipole matrix element $\langle z \rangle$ of this transition can be determined by using the relation [9]

$$I_A = \frac{\rho_s N(e^2 h/4\epsilon_0 m^* c)}{n_r^2 \sqrt{n_r^2 + 1}} f_{os}, \tag{2.5}$$

where I_A is the integrated absorption strength with a unit of [Absorbance-cm^{-1}], ρ_s is the two-dimensional electron density, N is the number of wells, m^* is the electron effective mass, and n_r is the refractive index of GaAs. The oscillator strength f_{os} is defined by

$$f_{os} = (4\pi m^* c/\hbar\lambda)\langle z \rangle^2, \tag{2.6}$$

where λ is the wavelength.

To calculate the absorption coefficient, the standard dipole approximation is used. The intersubband optical absorption coefficient α for the transition between the ground state and the first excited level can be expressed as [61]

$$\alpha = \frac{|e|\omega\mu c m^*}{n_r L_w \pi \hbar^2} \int_0^\infty dE_t \frac{\langle z \rangle^2 (f_1 - f_2)\hbar\gamma_{12}(E_t)}{(E_2 - E_1 - \hbar\omega)^2 + (\hbar\gamma_{12}(E_t))^2} \tag{2.7}$$

where $\langle z \rangle$ is the dipole matrix element given by

$$\langle z \rangle = \int_{-L_w/2}^{L_w/2} \psi_2^* z \psi_1 \, dz \tag{2.8}$$

and E_t is the transverse component energy given by

$$E_t = \hbar^2(k_x^2 + k_y^2)/2m^* \tag{2.9}$$

where μ is the permeability; n_r is the refractive index (for GaAs, $n_r = 3.27$); c is the speed of light in free space, and $\hbar\gamma_{12}(E_t)$ is the intersubband bandwidth. The Fermi level E_F can be determined from knowledge of the subband energies and the carrier concentration [20]

$$n_0 = \frac{m^* k_B T}{\pi \hbar^2 L_z} \sum_n ln[1 + exp(\frac{E_f - E_n}{k_B T})] \tag{2.10}$$

where L_w is the well width, and m^* is the electron effective mass.

2.3 Dark Current

The dark current is associated with the thermionic emission out of quantum wells and the tunneling component through the barriers. For the highly sensitive and background-noise-limited infrared photodetector (BLIP), all the dark current of the device arising from either thermionic emission or tunneling must be kept as small as possible in order to achieve the required signal-to-noise ratio (S/N) and detectivity D^*_{BLIP}. The GaAs/AlGaAs multiple quantum well detector is a majority-carrier device, and as such the noise is determined mainly by the fluctuation in the density of majority carriers within the device.

In order to calculate the dark current I_D, we first determine the density of electrons $n(V)$ which are thermally excited to the higher bands E_{SL} and E_{cont}, as a function of bias voltage V:

$$n(V) = (\frac{m^*}{\pi \hbar^2 L_p}) \int_{E_0}^{\infty} f(E) T(E, V) dE \tag{2.11}$$

where the first factor containing the effective mass m^* is obtained by dividing the two-dimensional density of states $(D(E) = m^*/\pi \hbar^2)$ by the superlattice period L_p (to convert it into an average three-dimensional density), and $f(E)$ is the Fermi distribution function given by

$$f(E) = [1 + exp(E - E_0 - E_f)/k_B T]^{-1} \tag{2.12}$$

and E_0 is the ground bound state in the enlarged quantum well, E_f is the two-dimensional Fermi level, and $T(E, V)$ is the bias-dependent tunneling current transmission factor of the superlattice barrier which is calculated by the transfer-matrix method to be discussed in Chapter 3. The equation above accounts for both the thermionic emission for $E > V_b$ and thermionically assisted tunneling for $E < V_b$. One can calculate the bias-dependent dark current $I_D(V)$, using the relation

$$I_D = n(V)ev(V)A \tag{2.13}$$

where

$$v(V) = \frac{\mu F}{[1 + (\mu F/v_s)^2]^{1/2}} \tag{2.14}$$

here e is the electronic charge, A is the device area, and $v(V)$ is the average electron velocity, μ is the mobility, F is the average external field, and v_s is the saturated drift velocity.

2.4 Superlattices and Minibands

The successful growth of superlattice structures by the molecular beam epitaxy (MBE) technique has made it possible for the development of novel potential profiles with unique electronic and optical properties. Most commonly used among these heterostructures are heterojunction superlattices, such as GaAs/AlGaAs, AlInAs/InGaAs/InP, doping (nipi) superlattices, modulation-doped superlattices, and strained layer and variably spaced superlattices.

The superlattice, as originally proposed by Esaki and Tsu [1], has found wide applications in many new device structures, such as photodetectors, transistors, and light emitting devices. The superlattice is an artificial one-dimensional periodic structure constituted by different semiconductor materials with a period less than 100 Å. When a semiconductor with a larger band gap is interspaced with another one of a smaller gap, the former acts as a barrier for electrons in the conduction band of the

latter. The most thoroughly studied material system as applied to superlattice is the GaAs/AlGaAs system owing to the relative ease in its fabrication as well as its close lattice matching. Under the application of a bias, carriers can tunnel through these structures provided that the wider gap AlGaAs layers are sufficiently thin. However, to optimize the current flow in a multiple quantum well or superlattice structure, the adjacent energy levels within the GaAs wells, arising from spatial quantization effects, must be aligned. Numerous experimental measurements have recently confirmed the presence of resonant tunneling in single, as well as multiple, quantum well structures. Optical absorption measurements have also independently verified the formation of superlattice minibands arising from the coupling of adjacent quantum states.

The formation of minibands is mainly attributed to the strong penetrations and interactions of the wave functions among the different quantum wells in the very short-period superlattices. To start with, let us first examine the strong coupling effect in a double-well case as shown in Figure 2.1 (a). As the barrier thickness is decreased, the exponentially decaying wave function in the barrier can have some finite value in the next well. Treating this wave function overlap as a perturbation, one finds the perturbation element in a double-well configuration given by [22],

$$V_{12} = < \phi_1|H|\phi_2 > = < \phi_1|V_2|\phi_2 > \tag{2.15}$$

where H is the electronic Hamiltonian, ϕ_1 and ϕ_2 are the unperturbed wave functions of single wells 1 and 2, and V_2 is the confining potential of well 2. Due to this interaction between the wells, the two degenerate well levels are split into a symmetric and antisymmetric compound wave functions with energies given by $(E_1 - V_{12})$ and $(E_1 + V_{12})$, respectively.

For N quantum wells, the N-degenerate levels give rise to a relative broad bands. The corresponding Bloch-like envelope wave function can be written as [23]

$$\phi_q^i(z) = \frac{1}{\sqrt{N}} \sum_n e^{iqnd} \chi_{loc}^i(z - nd) \tag{2.16}$$

where $\chi_{loc}^i(z - nd)$ is the ith wave function of the quantum well centered at $z = nd$ and q is the Bloch wave vector. Assuming a nearest-well interaction, the energy is

$$E = E_i + s_i + \Delta_i \cos(qd) \tag{2.17}$$

with

$$s_i = \int_{-\infty}^{+\infty} \chi_{loc}^i(z - d)V(z)\chi_{loc}^i(z - d)dz \tag{2.18}$$

$$\Delta_i = 2\int_{-\infty}^{+\infty} \chi_{loc}^i(z)V(z)\chi_{loc}^i(z - d)dz \tag{2.19}$$

where $2\Delta_i$ represents the bandwidth of the degenerate miniband.

The wave function coupling effect in superlattice introduces profound changes in the density of state distribution. When proceeding from a level structure of isolated well to minibands in a superlattice with sufficiently permeable barriers, we can follow the broadening in the density of states. It has a staircase character for the isolated well. Each level can be occupied by the number of electrons given by its degeneracy multiplied by the number of electrons in the wells. When significant tunneling becomes possible, each level splits into bands, and the staircase behavior (dashed steps) becomes somewhat softened (solid curve).

The dispersion of the N states in a band destroys the steepness of the square density of states and evolves into

$$\rho_n(E) = N\frac{m^*}{\pi\hbar^2}\cos^{-1}\left(\frac{E - E_i - s_i}{\Delta_i}\right) \tag{2.20}$$

Figure 2.1 (b) shows the broadened density of states (DOS) with the introduction of the superlattice structure.

Some calculations of the band structure of superlattice have been carried out in the envelope wave function approximation, using the Kane model to describe the band structure within each well and barrier. Basically, the bandwidth of miniband is a function of superlattice period (2a). Figure 2.2 shows that the miniband would become broader and broader as the superlattice period (2a) reduces. Bastard [24] has

shown that for $k_\perp = 0$, in the parabolic band approximation, the equation yield the values of q takes the simple Kronig-Penney form of the bound states

$$\cos qd = \cos k_A L_A \cosh \kappa_B L_B - \frac{1}{2}(1/\xi - \xi) \sin k_A L_A \sinh \kappa_B L_B \qquad (2.21)$$

with $\xi = m_A^* k_A / m_B^* k_B$. The solutions of unbound states (above the barrier) are similarly given by

$$\cos qd = \cos k_A L_A \cosh \kappa_B L_B - \frac{1}{2}(1/\xi + \xi) \sin k_A L_A \sinh \kappa_B L_B \qquad (2.22)$$

The two equations above can be solved graphically. The limiting cases of very thin layers, where the envelope wave function approximation tends to break down, can be calculated using LCAO method, which yields results similar to the envelope approximation as the layer thickness exceeds 20 $\mathring{A}$.

The minibands are separated by miniband gaps within the valley of the conduction band. Higher minibands could extend beyond the height of the potential barriers. In the plane of the superlattice layer, the electron eigenfunction experiences only the regular lattice periodicity. Therefore the dispersion relations $E(k_x)$ and $E(k_y)$ are much like those for the unperturbed lattice except for the mixing with the states in the z-direction. This results in lifting the lowest energy (at $k = 0$) of the $E(k)$ parabola above E_c of the bulk well material. The second miniband results in a second, shifted parabola, etc.

The $E(k)$ behavior in the minibands of the valence band is a bit more complicated, since we must distinguish between light and heavy holes which result in two sets of minibands. Considering excited states in the valence band, we observe a crossing of states between heavy and light hole bands. This results in a mixing and splitting between these states, making the top of the upper band light-hole-like, and its bottom part heavy-hole-like.

As the width of layers in superlattices becomes thinner and thinner, the superlattice structure finally disappears and is replaced by the electronic structure of a single

compound. The distinction between a true superlattice and a bulk semiconductor can be made when all band gaps between minibands disappear and the density of states increases monotonically from the band edge into the band.

To obtain the actual barrier height, it is important to know the conduction band edge offset, which is influenced by the substrate material and the deposition sequence. The periodic alternation of such layers produces a potential of same form described as the Kronig-Penney potential. The resulting eigenvalue spectrum is similar to the spectrum of free electrons exposed to the periodic potential of a crystal, except that now the periodic potential is imposed on Bloch electrons with an effective mass m^*, and the potential has a lower amplitude and a larger period length than the periodic potential in a bulk lattice.

Superlattice, used as a potential barrier, has an equivalent function just like that of bulk AlGaAs barrier. More importantly, it has many other unique features. Like the conventional quantum wells, the superlattice barrier quantum wells also involve the confinement of charge carriers and determination of energy eigenvalues and wave functions in the heterostructure. In principle, the short-period superlattice barrier can be approximately treated as one composition bulk material (i.e. AlGaAs) with a much lower effective barrier height ΔE_c, but the wave functions inside the quantum well remain basically the same.

Figure 2.3 shows the ground state wave function ϕ_0 and energy level E_{EW_0} of the enlarged well (EW). Due to the finite barrier potential, the tails of wave function extend into the cladding barrier regions. The broken line represents the wave function with the superlattice barrier, and solid line with uniform bulk barrier. The shapes of wave function are quite similar inside the quantum wells, but different in the barrier regions. A relative larger amplitude $|\phi_0|$ of the wave function is depicted in the superlattice barrier region, indicating that the tunneling process is more likely to take place in the superlattice structure than in the bulk barrier structure. Figure 2.4

shows the various ways to build a desirable quantum well through the implementation of the superlative barrier structures. By adjusting the superlattice parameters, a new type of quantum well with its unique properties can be obtained.

The most noticeable phenomenon is the coherent resonant tunneling (RT), which is also known as the Fabry-Perot effect. In the presence of negligible scattering of the electrons in the well, the negative differential resistance in the superlattice tunneling structure is accompanied by a coherent enhancement of the transmission, analogous to that occurring in an optical Fabry-Perot. In the case of a symmetric structure, after a transient in which the electron wave function builds up in the quantum well, an equilibrium is reached where the portion of the incident wave reflected by the first barrier is exactly cancelled by the fraction of the electron wave function leaking from the quantum well to the left. The net effect is a total transfer of electrons from the left to the right through the double barriers. In the case of coherent resonant tunneling, the peak transmission at resonance is given approximately by T_{min}/T_{max}, where T_{min} is the smallest among the transmission coefficients of the quantum well barriers.

In a superlattice, the barrier thickness becomes comparable to the carrier de Broglie wavelength. The wave functions of the individual wells tend to overlap each other due to the coupling effect. The tunneling probability for rectangular barriers can be estimated from the expression

$$T \simeq exp\left[-\sqrt{\frac{8m^*}{\hbar^2}(V(x)-E)}L_B\right] \qquad (2.23)$$

where m^* is the electron effective mass, ΔE_c is the conduction band offset, and L_B is the barrier thickness. The minibandwidth and state energies can be calculated rigorously by solving the Schrödinger equation.

The above picture assumes a perfect superlattice, with no thickness or potential fluctuations and no scattering by either impurities or phonons. In reality, one must contend with such fluctuations and with the unavoidable presence of scattering. Such effects tend to disturb the coherence of the wave function and the formation

of extended Bloch states which give rise to the miniband picture and have profound effects on perpendicular transport. One mechanism for smearing out the field dependent resonant tunneling features involves energy and momentum relaxing scattering processes [5,25]. The full width at half-maximum (FWHM) ΔF of the field dependent photocurrent is approximately given by $\Delta F = \hbar/ed\tau$, where d is the period of the superlattice and τ is the relaxation time of the momentum. It is believed that the field dependent transport characteristics are a combination of the resonant tunneling and the nonresonant tunneling process. Charge transport due to the sequential resonant tunneling is presumed to happen relatively fast with a quantum mechanical limit given by $\pi\hbar/\Delta E$ which is in the order of picosecond (ps). This value is near the same order as the limiting time constant of 5 - 10 ps for the intersubband relaxation [?].

Charge transport due to nonresonant tunneling should occur much slower than for the resonant tunneling case since it is forbidden in the sense that the carriers have tunneled into one of the energy gaps between the subbands of the adjacent well. The transmission probability T of an electron with energy E through a barrier of the potential profile $V(x)$ can be found by the WKB-approximation

$$T \simeq exp\left[\frac{-2}{\hbar}\int_{barrier}\sqrt{2m^*(V(x)-E)}dx\right] \tag{2.24}$$

where m^* is the electron effective mass.

One simple method to estimate the transmission time is by dividing the phase velocity $v_p = \sqrt{2E/m^*}$ of the electron by twice the well width L_w, which yields

$$\nu = \frac{1}{L_w}\sqrt{\frac{E}{2m^*}} \tag{2.25}$$

Multiplying the parameter ν by the transmission probability T from Eq. (2.24) we can obtain a reasonable nonresonant transmission time.

When one applies an electric field across the superlattice, the wave functions become localized since the translational symmetry of the superlattice with period d is destroyed. At low fields $eFd \leq 2\Delta$ (where 2Δ is the bandwidth of the miniband), the

states are still delocalized over several superlattice periods (for large enough coherence lengths). One simple model to describe the transport processes in this regime relies on an analogy with the bulk case [27,28]. The mobility $\mu_\perp$ for miniband conduction depends on the relaxation time $\tau_\perp$ in the following relation

$$\mu_\perp = \frac{e}{m_\perp^*} \tau_\perp \tag{2.26}$$

where the effective mass $m_\perp^*$ at the bottom of the miniband is approximately given by

$$m_\perp^* = \frac{\hbar^2}{d^2 \Delta} \tag{2.27}$$

The mobility decreases at higher fields ($eFd > 2\Delta$) because the carriers become completely localized and the nonresonant process becomes dominant. Under steady illumination, regions of negative differential photoconductivity can be observed.

2.5 Conclusion

In conclusion we have described the mathematical models of intersubband infrared transition, absorption coefficient, and the origins of dark current in the quantum well and superlattice structures. Since the whole derivations are based on general physical model, the equations can be used for different quantum well sizes and applied electric fields. We also described some properties of the composition superlattices, minibands, the equivalent superlattice barriers (SLBs) quantum wells. The basic miniband theory and charge transport mechanism are discussed. With the development of modern crystal epitaxial growth technology, superlattices have displayed an elegant illustration of the quantum mechanical behavior in semiconductor systems.

COUPLED WELLS

(a)

Ψ_1 Ψ_2

V_1 V_2

2 DEGENERATE STATES Ψ_1 AND Ψ_2

(b)

DENSITY OF STATES $\rho(E)$

$3D: m^* \sqrt{2m^* E} / \pi^2 \hbar^3$

d e

$2m^*/\pi\hbar^2$

a b

c

SUPERLATTICE

$m^*/\pi\hbar^2$

2D

O

ENERGY E
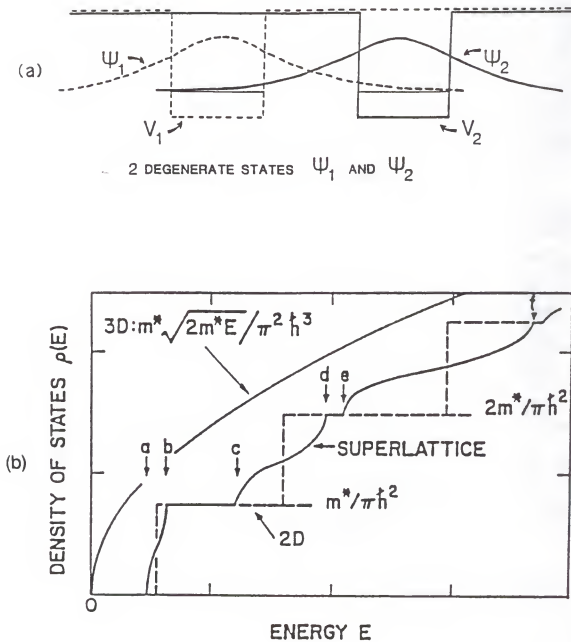
Figure 2.1 Two-dimensional broadenig effect in coupled quantum wells and super-
lattices (a) Coupling effect of wave functions between the quantum wells;
(b) Broadening of density of states (DOS), arisen from the strong cou-
pling effect in the superlattices.
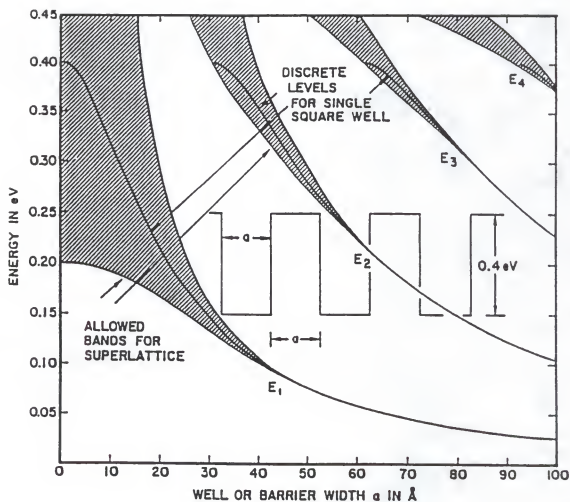
Figure 2.2 The existence of broad minibands in the short-period (2a) superlattice.
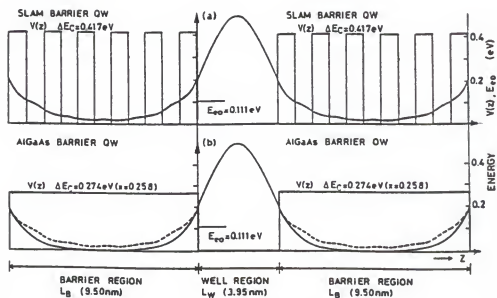
Figure 2.3 Comparason of a superlattice barrier and a bulk barrier quantum wells with the same effective barrier height. The shapes of wave functions inside the wells are almost identical except for the different behaviors in the barrier regions.

(a)
Symmetric QW

(b)
Asymmetric QW

(c)
Graded Barrier QW

(d)
Symmetric
SL-Barrier QW

(e)
Asymmetric
SL-Barrier QW 1

(f)
Graded
SL-Barrier QW 1

(g)
Stepped
SL-Barrier QW

(h)
Asymmetric
SL-Barrier QW 2

(i)
Graded
SL-Barrier QW 2

Figure 2.4 Schematic conduction band energy diagrams of various ways to construct
the quantum wells by applying superlattice barriers.

CHAPTER 3
CALCULATION OF ENERGY EIGENVALUES IN
QUANTUM WELLS AND SUPERLATTICES BY
TRANSFER MATRIX METHOD

3.1 Introduction

There are three different theoretical approaches for explaining the resonant tunneling phenomena in quantum well and superlattice structures. These include: (1) the Wentzel-Kramers-Brillouin (WKB) approximation [29,30], which is valid if the barrier energy varies slowly compared to the scale of the electron wavelength, (2) the Monte Carlo solution [31,32] of the semiclassic Boltzmann transport equation which assumes a quasi-particle picture of the electron, and (3) the transfer matrix approach which gives the transmissivity of the structure as a function of energy directly. The WKB approximation is not valid in the quantum well structures of interest, such as the narrow barriers, due to the rapid potential changes in these structures. For the WKB approximation to be valid, the change in a wavelength in the potential energy relative to the kinetic energy must be small. In other words, the wavelength must be small compared to the distance over which the momentum changes appreciably or 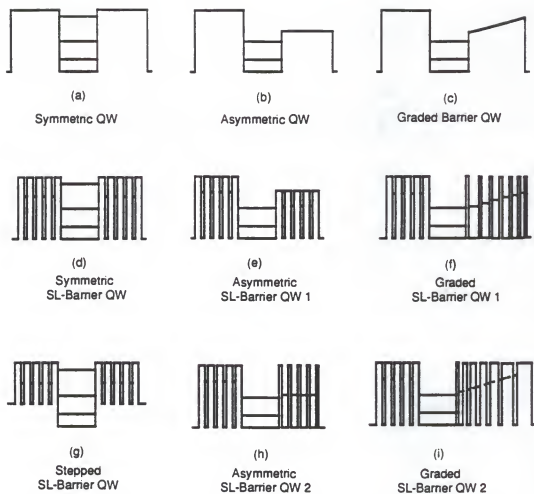over which the potential changes appreciably. This condition is not satisfied in structures in which the barriers are narrow, especially at low-incident carrier energies. The Monte Carlo approach is useful since it includes phonon scattering but does not easily lend itself to the calculation of the structure's transparency. Even with the popular variational method, it does not give the correct value of the wave function outside of the well, nor predict the lifetime of quasi-bound states. Solution of the energy levels and wave functions with the variational method depends on the choice of trial function, which becomes very difficult for structures involving more than one

23

quantum well, and also for the graded potential structures. It is well known that the variational method is not convenient for states other than the ground state.

Considering the limitations cited above, we have successfully applied the matrix technique to solve the eigenvalue states and transmission of quantum well and superlattice structures. The matrix method is one of the most powerful and straightforward techniques in investigating the quantum well and superlattice structures. It overcomes all the problems cited above. It can also be applied to analyze *any* arbitrary potential profiles, including asymmetric, graded, and parabolic quantum well structures. Unlike conventional methods, it can simultaneously calculate the eigenstate energies, the lifetime of quasi-bound states, and predict the influence of electric field upon the lifetime as well. It is able to give not only the correct values of wave functions inside the quantum wells, but also the values outside the wells, either with or without external electric field. Due to its interactive properties, it becomes even more powerful when dealing with superlattice (SL) and multi-quantum well (MQW) structures. Therefore, we have employed the transfer matrix method in this work to design and analyze the III-V quantum well and superlattice infrared photodetectors.

3.1 Theory of Transfer Matrix Method

It is well known that the time-independent one-electron Schrödinger equation in a quantum well can be expressed as

$$\frac{d^2\psi}{dz^2} + \frac{2m}{\hbar^2}[E - V(z)]\psi = 0 \tag{3.1}$$

where m is the mass, E and ψ represent the energy eigenvalue and eigenfunction of the bound state, respectively. The potential function, V(z), under bias condition, which is given by

$$V(z) = V_0 + q\mathcal{E}z \tag{3.2}$$

where $\mathcal{E}$ is the electric field, and q is the electronic charge.

The carrier wave in each of the multiquantum well and superlattice potential regions consists of two components propagating in forward and backward directions, respectively.

$$\psi_i = \psi_i^+ e^{-i\Delta_i} e^{+ik_i} + \psi_i^- e^{+i\Delta_i} e^{-ik_i} \tag{3.3}$$

where

$$\Delta_1 = \Delta_2 = 0, \quad \Delta_i = k_i(d_2 + d_3 + \cdots + d_i) i = 3, 4, \cdots, N \tag{3.4}$$

$$k_i = \left[\frac{2m^*}{\hbar^2} (E - V_i) \right]^{1/2} \tag{3.5}$$

where ψ_i^+ and ψ_i^- represent the magnitudes of the particle wave functions propagating along the $+x$ and $-x$ directions, respectively.

Since ψ and $d\psi/dx$ are continuous at the boundaries, we obtain

$$\psi_i^+ = (e^{i\delta_i}\psi_{i+1}^+ + r_i e^{i\delta_i}\psi_{i+1}^-)/t_i \tag{3.6}$$

$$\psi_i^- = (r_i e^{-i\delta_i}\psi_{i+1}^+ + e^{-i\delta_i}\psi_{i+1}^-)/t_i \tag{3.7}$$

here the recurrence relation may be written in matrix form as

$$\begin{pmatrix} \psi_i^+ \\ \psi_i^- \end{pmatrix} = \frac{1}{t_i} \begin{pmatrix} e^{i\delta_i} & r_i e^{i\delta_i} \\ r_i e^{-i\delta_i} & e^{-i\delta_i} \end{pmatrix} \begin{pmatrix} \psi_{i+1}^+ \\ \psi_{i+1}^- \end{pmatrix} \tag{3.8}$$

where

$$r_i = \frac{(m_{j+1}^*/k_{i+1}) - (m_j^*/k_i)}{(m_{j+1}^*/k_{i+1}) + (m_j^*/k_i)} \tag{3.9}$$

$$t_i = \frac{2(m_{j+1}^*/k_{i+1})}{(m_{j+1}^*/k_{i+1}) + (m_j^*/k_i)} \tag{3.10}$$

$$\delta_i = k_i d_i \tag{3.11}$$

Thus, we have

$$\begin{pmatrix} \psi_1^+ \\ \psi_1^- \end{pmatrix} = S_1 \begin{pmatrix} \psi_2^+ \\ \psi_2^- \end{pmatrix} = S_1 S_2 \begin{pmatrix} \psi_3^+ \\ \psi_3^- \end{pmatrix} = \cdots = S_1 S_2 \cdots S_N \begin{pmatrix} \psi_{N+1}^+ \\ \psi_{N+1}^- \end{pmatrix} \tag{3.12}$$

Since there is no forward propagating component in the last medium, i.e. $\psi_{N+1}^- = 0$, one can find $\psi_j^+ (j = 2, 3, \cdots, N+1)$ in terms of E_1^+, where j represents the layer

region to be investigated. If we calculate the quantity $\eta(\beta) = \frac{\psi_j^+}{\psi_1^+}$ as a function of E, then we can obtain certain resonance peaks. It can be shown [33-35] that the resonance curve has a Lorentzian distribution which corresponds to each bound state and quasi-bound state of the form

$$\left|\frac{\psi_j^+}{\psi_1^+}\right|^2 = \frac{\sigma}{(E - E_b')^2 + \Gamma^2} \tag{3.13}$$

where

(1) $E = E_b'$ indicates the position of the peak (eigenvalue of the bound state),

(2) 2Γ is the full width at half maximum (FWHM). Γ would approach to zero for bound states, and to a nonzero value for the quasi-bound states.

(3) $\tau = h/4\pi\Gamma$ is the lifetime of the quasi-bound states. We calculate the ratio $|\psi_j^+/\psi_1^+|$ inside each of the wells so that all energy levels and related properties can be obtained, where j represents the well region of interest.

(4) σ/Γ^2 represents the peak value of relative electron density distribution.

(5) Similar results can be obtained outside the well, provided that j in this case is the potential value inside the barrier or any other adjacent well.

3.3 Conclusion

In conclusion, we have discussed a transfer matrix method for solving the two-dimensional quantum well and superlattice structures. The 2×2 matrix approach is a simple and straightforward technique. It can simultaneously give the carrier transmission coefficient, relative density of states, eigenstate energies, and carrier lifetimes in the multiple heterostructure quantum wells and superlattices. It provides a great deal of design flexibility and calculation capability.

CHAPTER 4
FIGURES OF MERIT

4.1 Introduction

Photoconductivity is a well understood subject in solid-state physics. Photoconductivity has been widely used in probing the defects in the structure of solids and a variety of applications in infrared camera tubes, electrostatic photography, light amplifiers, electrical switches, and photon detections.

The performance of a photodetector may be evaluated in terms of its spectral responsivity, signal to noise ratio, equivalent noise power, and detectivity. A photoconductor exhibits a change in conductance when photons are impinging upon it. The absorbed photons increase the conductance of photoconductor by generating excess charge carriers in the photodetector. The excess carriers cause an increase in the conductivity of the semiconductor, which is called the photoconductivity.

4.2 Photoconductive Detection Mechanism

In an extrinsic semiconductor, conductivity is associated with just one type of carriers, which we choose to be the electrons for this discussion. The conductivity can be written as

$$\sigma = n_0 q \mu_e \tag{4.1}$$

where n_0 is the free carrier concentration, and μ is the electron mobility. If Δn is the concentration of excess electrons generated by the absorption of photons, then the conductivity is given by

$$\sigma_n = q(n_0 + \Delta n)\mu_e \tag{4.2}$$

The effect of the excess carrier concentration is to increase the conductivity, and hence to produce a viable detection mechanism for the absorbed optical radiation. The steady state conductivity can be expressed as

$$\sigma_n = \sigma_0 + \Delta\sigma \tag{4.3}$$

where σ_n is the conductivity under dark condition, and $\Delta\sigma$ is the photoconductivity given by

$$\Delta\sigma = q\Delta n\mu_e \tag{4.4}$$

The excess carrier concentration, Δn, generated by the absorbed photons can be expressed as

$$\Delta n = \frac{\eta\Delta\Phi_0\tau_L}{A \cdot W} \tag{4.5}$$

where η is the quantum efficiency, $\Delta\Phi_0$ is the incident photon flux (photon/sec), τ_L is the electron lifetime, A is the detector area, and W is the detector active layer thickness.

Equation (4.5) assumes that a change in the number of carriers per unit volume is due to photo-generated excess carriers with an average lifetime (τ_L) in a detector volume of AW. The quantum efficiency η is defined as the number of photocarriers generated in the detector per incident photon within the spectral sensitivity of the device. Thus, the relative change in conductivity can be written as

$$\frac{\Delta\sigma}{\sigma_0} = \frac{q\mu_e}{\sigma_0}\frac{\eta\Delta\Phi_0\tau_L}{A \cdot W} \tag{4.6}$$

This is the change in conductivity due to the presence of incident photons ($\Delta\Phi_0$) in the detector's active region.

Sometimes, it is more convenient to use resistance from an engineering viewpoint. By this means, the resistance of the detector can be expressed as

$$R_d = \frac{W}{\sigma A} \tag{4.7}$$

The differential resistance of the detector can be written as

$$dR_d = -\frac{W d\sigma}{\sigma^2 \sigma A} = -R_d \frac{d\sigma}{\sigma} \tag{4.8}$$

This can be considered as the resistance having an opposite slope to that of the relative change in conductance, and hence the negative sign in the expression.

By substituting Eq. (4.7) into Eq. (4.8), the change in resistance due to incident photon flux is

$$dR_d = -R_d \frac{q\mu_e}{\sigma} \frac{\eta \Delta \Phi_0 \tau_L}{AW} \tag{4.9}$$

The photon signal flux $(\Delta \phi_0)$ can be expressed in watts of radiant power assuming that the incident photon signal is monochromatic:

$$\Delta \phi_0 = \frac{P_0}{hc/\lambda} \tag{4.10}$$

where P_0 is the incident signal radiant power (W), h is the Planck's constant, c is the speed of light, and λ is the wavelength of optical radiation. The output signal (V_0) across the load resistor is

$$V_0 = \frac{V_b R_L}{R_d + R_L} \tag{4.11}$$

where R_d is the load resistor, R_L is the load resistor, and V_b is the bias voltage. The change in output voltage due to a change in detector resistance (R_d) is found as

$$dV_0 = \frac{-V_b R_L dR_d}{(R_d + R_L)^2} \tag{4.12}$$

where dV_0 is the ac-voltage signal, caused by incident signal photons, superimposed on the dc voltage V_0. Thus, the change in resistance is used to produce an electrical signal that is dependent on the incident irradiance and external bias.

4.3 <u>Figures of Merit</u>

Figures of merit are physical parameters which are often used to evaluate the performance characteristics of a detector over a specified spectral range. The detector figures of merit are important parameters which are used to determine the detector performance limitation. To design a detector system, it is important to know the definitions and limitations of the commonly used figures of merit, such as spectral responsivity (R_λ), noise equivalent power (NEP), and detectivity (D^*).

4.3.1 <u>Spectral Responsivity</u>

A common figure of merit that applies to all detectors with electrical output is responsivity. Responsivity is the ratio of the output current or voltage (usually in amperes or volts) to the radiant power input (in watts), which can be defined as

$$R_v = \frac{dV_0}{\phi_{ph}(\lambda)} \tag{4.13}$$

where λ is the photon wavelength, dV_0 is the output voltage given by Eq. (4.12), and $\phi_{ph}(\lambda)$ is the spectral photon radiant power incident on the detector.

The spectral voltage responsivity for the photoconductive detector can be expressed as

$$R_v = \frac{\eta q I \lambda \tau_L \mu_e}{\sigma A_d hcW} \frac{R_L R_d}{R_L + R_d} \qquad (V/W) \tag{4.14}$$

From Eq. (4.14), it is noted that the voltage responsivity is a function of the load resistance/detector resistance in parallel. The current responsivity expression can be derived by using the relationship that $dI = R_L dV$. Thus, the expression for the current responsivity becomes

$$R_i = \frac{\eta q I \lambda \tau_L \mu_e}{\sigma A_d hcW} \frac{R_d}{R_L + R_d} \qquad (A/W) \tag{4.15}$$

where η is the quantum efficiency, q is the electron charge, λ is the wavelength of light, τ_L is the carrier lifetime, μ_e is electron mobility, σ is detector conductivity, A is the effective area of detector, and W is the active layer thickness.

4.3.2 Noise Equivalent Power (NEP)

The noise equivalent power of a detector is the required power incident on the detector to produce a signal output equal to the rms noise output. Since the current signal output is

$$i_{ph} = R_i \phi_{ph} \tag{4.16}$$

the signal-to-noise ratio can be written as

$$S/N = \frac{R_i \phi_{ph}}{i_n} \tag{4.17}$$

From Eq. (4.17), the NEP is the incident radiant power, ϕ_{ph}, for a signal-to-noise ratio of 1, which is given by

$$NEP = \frac{i_n}{R_i} \tag{4.18}$$

where i_n is the root-mean-square noise current in amperes and R_i is the current responsivity in amperes per watt.

4.3.3 Detectivity D^*

A more useful figure of merit is the normalized detectivity D^*, which normalizes the detector area and bandwidth:

$$D^*(\lambda, f) = \frac{\sqrt{A_d \Delta f}}{NEP} = \frac{\sqrt{A_d \Delta f}}{i_n} R_i \tag{4.19}$$

where either spectral or blackbody NEP may be used to define spectral detectivity. The advantage of D^* as a figure of merit is that it is normalized to an active detector area of 1 cm^2 and noise bandwidth of 1 Hz. Therefore, D^* may be used to compare directly the merit of detectors of different size whose performance was measured using different band widths.

4.3.3 Background-Noise-Limited Infrared Photodetector (BLIP)

In the long wavelength spectral region ($\lambda > 3\mu m$), infrared photodetectors can achieve background photon-limited performance, which is termed BLIP. If the photon

irradiance incident on a photon-noise-limited detector is due primarily to background photons, then the detector is said to be a background-noise-limited infrared photodetector. For this BLIP operation the spectral NEP can be expressed as

$$NEP(\lambda, f) = \frac{2hc}{\lambda} \left[\frac{E_{ph}^B A \Delta f}{\eta} \right]^{1/2} \qquad (4.20)$$

where h is the Planck's constant, c is the speed of light, E_{ph}^B is the background photon irradiance, and η is the quantum efficiency. The corresponding BLIP operation spectral detectivity D^* of a photoconductor is

$$D^*(\lambda, f) = \frac{\sqrt{A_d \Delta f}}{NEP} = \frac{\lambda}{2hc} \sqrt{\frac{\eta}{E_{ph}^B}} \qquad (4.21)$$

4.4 Photoconductive Gain

One of the advantages of a photoconductor over a p-n junction (photovoltaic) type of detector is that a large photocurrent gain G can be obtained in a photoconductive mode. If one rearranges the terms in the current responsivity expression derived for the photodetector in the previous section, the spectral responsivity R_i can be rewritten as

$$R_i = \frac{\eta q \lambda}{hc} Q G \qquad (A/W) \qquad (4.22)$$

where

$$Q = \frac{R_L R_d}{R_L + R_d} \qquad (4.23)$$

and

$$G = I A_d \tau_L \mu_e \sigma W \qquad (4.24)$$

The term G is called the photoconductive gain, which can also be written as

$$G = \frac{\tau_L \mu_e F}{W} \qquad (4.25)$$

where τ_L is the electron lifetime, μ_e is the electron mobility, W is the detector thickness (interelectrode spacing), and F is the electric field strength in detector (V cm^{-1}).

The transit time (τ_t) of photogenerated electron across the photoconductor can be expressed as

$$\tau_t = \frac{W}{\mu_e F} = \frac{W}{v_d} \tag{4.26}$$

The magnitude of the photocurrent is determined by the drift velocity across the semiconductor (interelectrode spacing) and the carrier lifetime. Conceptually, one can think about the photogenerated carrier having a lifetime long enough to traverse across the semiconductor electrodes. If the carrier lifetime is long, the carrier may traverse the detector several times before it recombines. Thus the photoconductive gain can be expressed as the ratio of carrier lifetime (τ_L) to detector transit time (τ_t)

$$G = \frac{\tau_L}{\tau_t} \tag{4.27}$$

4.5 Summary

In summary, we have reviewed the photoconductive detection mechanism and the figures of merit for the photoconductive detectors. The important figures of merit, such as the spectral responsivity R, the noise equivalent power NEP, and the detectivity D^* are defined. These parameters are extremely important and useful in specifying the performance of infrared photodetectors.

CHAPTER 5
METAL GRATING-COUPLED BOUND-TO-MINIBAND
TRANSITION GaAs/AlGaAs QUANTUM WELL
SUPERLATTICE INFRARED DETECTOR

5.1 Introduction

A principal concern with quantum well infrared photodetectors (QWIPs) is to obtain high detectivity and low dark current at high operating temperature. At high temperatures (77 K or higher), the detectivity of QWIPs is significantly reduced because of the existence of large dark current and its associated thermal noise. In the conventional bound-to-continuum transition GaAs QWIP, the main dark current consists of thermionic emission contribution arising from the Maxewell-Boltzmann tail of Fermi-Dirac distribution above the AlGaAs barrier. To reduce dark current, a higher barrier potential is needed to suppress the thermionic emission contribution.

The introduction of superlattice and quantum well technology makes it possible to design and construct various novel quantum devices which was impossible to make earlier. Several long wavelength infrared (LWIR) detectors based on bound-to-bound [10,11], bound-to-virtual excited state [12], bound-to-continuum 13,14], and miniband-to-miniband [6,7] state transition in the multiple quantum well structures have been extensively investigated.

Here we focus on a class of long wave infrared (LWIR) detectors using the enlarged quantum well and short-period superlattice barrier structures. The infrared detection mechanism is based on the bound-to-miniband (BTM) transition and superlattice miniband transport. A high superlattice barrier potential is used to suppress the thermionic emission contribution to the dark current.

The creation of enlarged quantum wells and resonant miniband transport structure, which is known as bound-to-miniband (BTM) transition, offers a great deal of design flexibility and improved device performance. Figure 5.1 shows the schematic conduction band energy diagram of the BTM transition GaAs/AlGaAs QWIP. The intersubband transition takes place from the localized bound ground state E_{EW_1} in the enlarged wells (EWs) to the resonant-coupled miniband state E_{SL} of the superlattice (SL) barrier. The absorption region of the detector consists of GaAs EWs cladded by the AlGaAs/GaAs superlattice (SL) barriers at both sides. The physical parameters of the quantum wells and superlattices are chosen so that there are only two levels in the EW region, and the first excited level E_{EW_1} of the EW is merged and lined up with the ground level miniband E_{SL} of the SL on both sides of the GaAs quantum well to achieve a large oscillation strength f and intersubband absorption coefficient α. Since the superlattice has a relatively thin barrier, the photoexcited electrons can easily tunnel through the superlattice and transport along the aligned miniband, which are then collected by the external ohmic contacts.

5.2 Sample Preparation

The AlGaAs/GaAs multiple quantum well (MQW)/superlattice (SL) layer structure was grown on a semi-insulating (S.I.) GaAs substrate using molecular beam epitaxy (MBE). A 1 μm thick GaAs buffer layer of 2.0×10^{18} cm^{-3} was first grown on a S.I. GaAs substrate, followed by the growth of a 40-period of GaAs quantum wells with a well width of 88 Å and a dopant density of 2.0×10^{18} cm^{-3}. The barrier layer on each side of the GaAs quantum well consists of a 5-period of undoped $Al_{0.4}Ga_{0.6}As$ (58 Å) /GaAs (29 Å) superlattice layers which were grown alternatively with the GaAs quantum wells. Finally, an n^+-GaAs cap layer of 0.45 μm thick and dopant density of 2.0×10^{18} cm^{-3} was grown on top of the MQW layer structure to facilitate ohmic contact.

5.3 Theory, Experiments and Discussions

In order to understand the mechanism of bound-to-miniband transition, a numerical calculation of the relative density of states $D(E) = C \; |\psi(E)|^2$, where C is a constant, for different potential energy E was performed for the multiple quantum well/superlattice layers by the matrix method. For simplicity, parabolic energy band relation and an effective mass $m^* = 0.0665 m_0$ were assumed in the calculation. Results are shown in Figure 5.2(a). One finds that a broad miniband E_{SL} structure was formed in the quantum well and the first excited state $E_{EW_1} = 163$ meV is merged with the superlattice miniband E_{SL}. The ground state is at $E_{EW_0} = 42$ meV. The Fermi level E_f was found to be 68 meV above the ground state E_{EW_0}. The exchange energy shift [36-38] due to the electron-electron interaction is estimated to be $E_{xch} = 18$ meV at T = 20 K, respectively. Outside the quantum wells, the first continuum state is about 4 meV above the barrier ($E_{cn_1} = 326$ meV), and the second continuum state E_{cn_2} is 48 meV higher than the first continuum state. A large energy separation $E_{cn_1} - E_{EW_0} - E_{xch} = 300$ meV is used to suppress the thermionic emission [39,40].

Figure 5.3 shows the absorption spectral curve of the sample measured at T = 300 K by using a Fourier transform infrared (FTIR) spectroscopy at the Brewster's angle. The absorption peak is centered at $\lambda_p = 9.6$ μm. The measured peak absorbance A = -$\log_{10}$ (transmission) was found to be about 7×10^{-2}. The bandwidth broadening, slightly larger than the expected value of 16 meV, might be attributed to the result of interface roughness and spatial inhomogeneities in the well and superlattice widths [9], high temperature influence, and higher subband lifetime broadening effect. Considering the peak wavelength position λ_p and the uncertainties such as band gap discontinuities, actual electron density distribution, true well shape, interactions between the electrons and phonons, electrons and electrons, the experimental results are in good agreement with the theoretical prediction.

Device characterization was carried out in a liquid-helium cryogenic dewar. An HP4140B semiconductor parameter analyzer was used to measure the dark current vs. voltage (I-V) curves. Figure 5.4 displays a semi-log scale plot of the I-V curves obtained for temperatures between 42 and 85 K. Under dark conditions, electrons can transfer out of the wells and produce the observed current mainly via two mechanisms. One is the thermionic emission out of the quantum wells, which is the dominant component of the dark current for the low barrier structure detectors at low bias, especially at higher temperatures. The other is the thermally generated carriers tunneling through the superlattice miniband. In the bound-to-miniband transition structure, we chose a high value of 'Al' composition, $x = 0.4$, which gave the barrier potential as high as $\Delta E_c = 322$ meV ($\sim 65\% \Delta E_g$). The highly localized and heavily populated ground state E_{EW_0} is deeply resided in the enlarged quantum well sandwiched between the large potential superlattice barrier regions, and far from the continuum states above the barrier. Therefore, carriers due to thermionic emission out of the quantum wells in the new QWIP's can be greatly reduced. On the other hand, the thermal generated carriers tunneling through the E_{EW_1} and the miniband can also be reduced by adjusting the bandwidth [41,42] of the miniband E_{SL}. For our quantum well device with an area $A = 4 \times 10^{-4}$ cm^2 and a doping concentration $n_d = 2.0 \times 10^{18}$, the dark current I_d was found to be around 8×10^{-9} A at $V_b = 0.2$ V and T = 68 K, and 9×10^{-8} cm^{-3} A at T = 77 K, respectively.

To enhance the light coupling efficiency to the quantum wells, we developed a planar transmission metal grating coupler [43] for the top illumination, which consists of regularly spaced metal grating fingers. Its periodicity Λ is chosen so that the phase matches the peak wavelength of the spectral response (blazing wavelength λ_B) of the detector. The metal grating was deposited by using E-beam evaporation of AuGe-Ni-Au materials. A highly efficient grating pattern deposited on the top surface of the detector mesa structure for the front surface illumination was obtained by using

a new planar grating with a periodicity $\Lambda = 5$ μm and ratio factor $t/\Lambda = 0.4$, where t is the metal strip width. The photocurrent was measured as a function of temperature, polarization direction, radiation wavelength, using a CVI Laser Digikrom 240 monochromator and an ORIEL ceramic element infrared source. Due to the very large device resistance ($\geq 500 K\Omega$ in the temperature range from 6 K to 77 K) and the small values of dark current I_d present in the device, the short-circuit measurements were used to determine the photocurrent I_{ph}. Figure 5.5 shows the normalized measured responsivity curve versus wavelength for the detector, which shows a peak spectral response at 8.9 μm at T = 20 K. In the inset of Figure 5.5, we also show the cross sectional view of a top illuminated metal grating coupled QWIP's used in this study with a periodicity of 5 μm. A maximum responsivity $R_\lambda = 0.54$ A/W was obtained at $V_b = 1.2$ V. As expected, the device responsivity R_λ increases with the applied bias voltage from $V_b = 0$ to $V_b = 0.6$ V. For $V_b > 0.6$ V, the photocurrent becomes saturated. A maximum operation bias at 1.8 V was obtained, and the photocurrent was found to decrease rapidly beyond 1.8 V, corresponding to the onset of the misalignment between the quasi-bound state levels and the superlattice miniband. The conduction mechanism for $V_b \geq 1.8V$ is due to phonon assisted tunneling (or hopping conduction). Further increase in the applied bias voltage will result in a strong decrease of the detector responsivity, which is consistent with the fact of a total misalignment of the minibands in the EWs and the superlattice barrier layers. We also measured the temperature dependence of the responsivity, and found that the responsivity was slightly decreased as the temperature increased. However, the change was small, and the responsivity still retained a peak value of $R_\lambda = 0.38$ A/W at $V_b = 1.2$ V, and $R_\lambda = 0.23$ A/W at $V_b = 0.2$ V and at T = 77 K.

It is worthwhile mentioning that a relatively large photocurrent was observed even at zero bias. One reason for this may be arisen from the space charges built up inside the superlattice layers. Another important mechanism could be due to

the strongly coupled coherent states—miniband transport in the superlattice structure. Since a large portion of the electron wave functions in the superlattice region is overlapped and the discrete quantum levels of the different superlattice layers are so closely packed, a strongly degenerate miniband is formed in the superlattice. There exists large coupling effects among these states. In other words, the excited electrons in the miniband are co-governed and shared by different quantum wells in the superlattice region, and the resonant tunneling can easily take place along the miniband. Therefore, the low bias operation, or the zero bias (dual-mode) condition can be realized in such a short period superlattice composed photoconductive detector. Similar phenomena were also observed in the different superlattice devices [5-7] even without grading layer [44].

From the measured responsivity and dark current, we can calculate the detectivity D^* of the detector using the expression

$$D_\lambda^* = R_\lambda (A\Delta f)^{1/2} / (4eI_d G\Delta f)^{1/2} \tag{5.1}$$

where A is the effective area of the detector, G is the optical gain, which can be evaluated from $R_\lambda = \eta(\lambda/1.24)G$ and $\eta = (1/2)(1 - e^{-2\alpha l})$, and Δf is the bandwidth. For $V_b = 0.2$ V, we found $D^* = 1.6 \times 10^{10}$ cm$\sqrt{Hz}$/W at $\lambda = 8.9$ μm and T = 77 K. By optimizing the device parameters further improvements in detector performance can be realized in a GaAs/AlGaAs MQW IR detector.

The bound-to-miniband (BTM) transition detection scheme offers a great deal of flexibility in detector design and manufacture. It has received a lot of industrial attention for its potential infrared imaging applications. Extensive work has been conducted at Martin Marietta Laboratories in developing high quality 128 × 128 long wavelength infrared (LWIR) detector array systems by using the BTM transition scheme. The arrays consist of 30 periods of enlarged wells and superlattice barriers. Pixels were 40×40 μm on 50 μm centers. The peak wavelength is at $\lambda_p = 9.5$ μm, with a full width at half maximum (FWHM) of 1.5 μm. At a bias of -3.0 V the peak

responsivity was 50 mA/W, yielding a peak $D^* = 4 \times 10^9$ cm Hz$^{1/2}$/W at T = 80 K. The hybridized focal plane array (FPA) had an uncorrected response nonuniformity of 18% and dark current non-uniformity of 20 - 30%. The pixel operability was greater than 99%. The noise-equivalent temperature difference of the array was about NEΔT = 0.1 K, at T = 60 K. With the improvement of readout electronics, a single pixel limited NEΔT $\leq$ 0.01 K is achievable.

5.3 Conclusion

In conclusion, we have demonstrated a novel GaAs/AlGaAs multiple quantum well infrared photodetector (QWIP) using the bound-to-miniband transition, resonant tunneling, and effective mass filtering mechanisms. The new structure also shows the advantages of large intersubband absorption and dual mode operation. With high detectivity, low bias operation, and grating coupled surface illumination, the GaAs QWIPs can be used for high quality detector arrays and infrared imaging sensors.
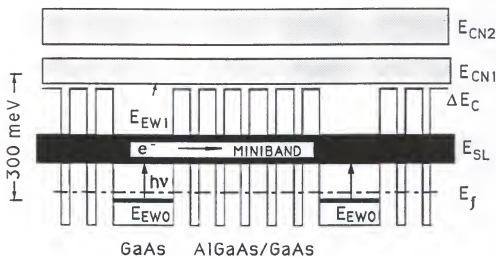
Figure 5.1 The energy band diagram for the bound-to-miniband transition followed by coherent superlattice miniband transport. The first excited level E_{EW_1} of quantum well is aligned with the miniband E_{SL} of the superlattice to achieve a large absorption. The continuum states E_{cn_i} (i = 1, 2, $\cdots$)are "lifted" up away from the heavily populated ground state E_{EW_0} to reduce the thermionic emission.
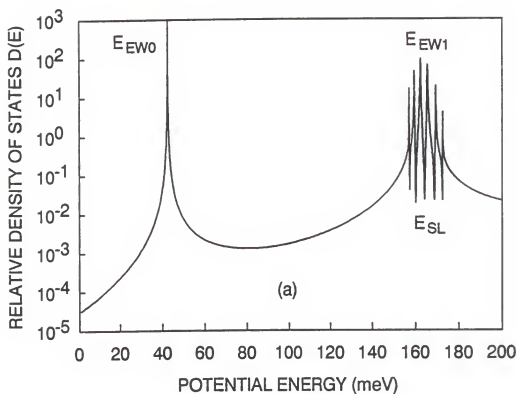
Figure 5.2 Calculated energy eigenvalues and relative density of states $D(E)$ vs. electron potential energy E in the enlarged quantum well (EW). A broad miniband E_{SL} was formed in the quantum layer structure by using the superlattice barriers.
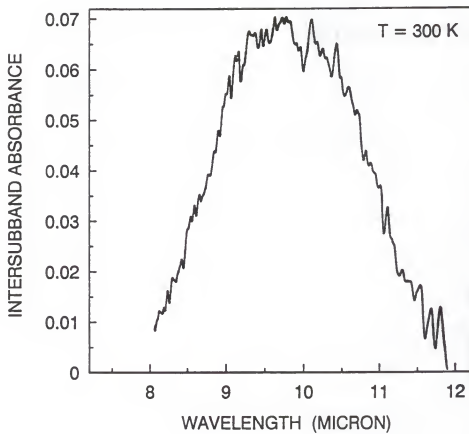
Figure 5.3 Measured room temperature (T = 300 K) intersubband absorbance vs. wavelength by the Fourier transform infrared (FTIR) spectroscopy at the Brewster's angle.
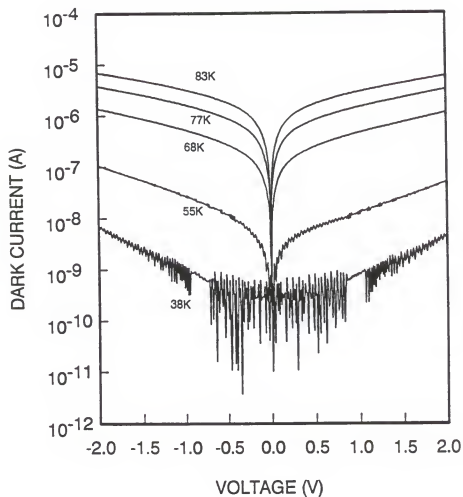
Figure 5.4 Plot of dark current vs. applied bias at different temperatures. A strong negative differential resistance (NDR) was obtained at a low temperature, comfirming the existence of coherent miniband transport and resonant tunneling
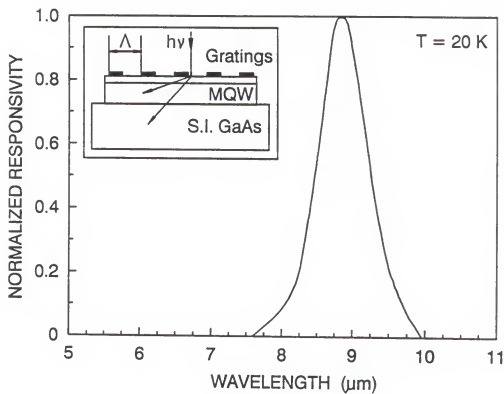
Figure 5.5 Measured spectral responsivity of the QWIP with a planar metal grating coupled top illumination at T = 20 K. The peak wavelength is at $\lambda_p =$ 8.9μm. A grating periodicity $\Lambda = 5\mu$m and ohmic contact material AuGe-Ni-Au was used for the study.

CHAPTER 6
LARGELY ENHANCED BOUND-TO-MINIBAND ABSORPTION IN
AN InGaAs/AlGaAs QUANTUM WELL WITH SHORT-PERIOD
SUPERLATTICE InAlAs/InGaAs BARRIER

6.1 Introduction

In addition to the study of the intersubband transition properties of multiple
quantum well in the GaAs/AlGaAs material system, we also investigated the InP
lattice-matched AlInAs/InGaAs material system.

The GaAs/AlGaAs system is the most studied material system [1-15], for some
applications there is considerable interest in InP lattice-matched InAlAs/InGaAs
quantum well and superlattice system [45-47]. First, the InAlAs/InGaAs quantum
well has a small effective mass $m^* = 0.042 \ m_0$, and the electron has a relatively
larger drift velocity v_{dr} and much shorter transition time t_{tr}, which is attractive for
many high-speed applications. Second, a photocurrent gain G $(=\tau/t_{tr})$ much greater
than unit can be obtained in the InAlAs/InGaAs superlattice detector structures,
which would significantly increase the quantum efficiency of long wavelength QWIPs.
Third, the higher barrier is particularly useful in suppressing the noise due to electron
thermionic emission out of quantum wells.

A study conducted at AT&T Bell Laboratories shows that intersubband absorp-
tion in InAlAs/InGaAs multiquantum well can be tuned to $3 - 5 \ \mu m$ [45]. The
small well width $L_w = 30 \ \mathring{A}$ bound-to-continuum state transition has a compara-
ble integrated absorption strength to that of a relatively wider well width $L_w = 50$
$\mathring{A}$ bound-to-bound intersubband absorption due to the broad continuum minibands
above the barriers. In reviewing the facts that small effective electron mass m^* and the

46

large energy band discontinuity ($\Delta E_c = 500$ meV), there is a great potential of using AlInAs/InGaAs material system for a much longer wavelength application. The new bound-to-miniband transition scheme may provide an alternative approach in designing the novel quantum well devices, which suggests that 10 μm or longer wavelength infrared detectors can obtained among most of the III-V material systems, including AlInAs/InGaAs, regardless of their energy band offset difference. We will also show that a wide well and broad miniband can be realized in the bound-to-miniband transition scheme which will be advantageous in obtaining a large integrated intersubband absorption strength in the multiquantum well/superlattice structures.

6.2 Theory and Experiments

In this section we report a detailed study of long wavelength infrared intersubband absorption based on bound-to-miniband transition in InAlAs/InGaAs multiple quantum well and superlattice structure. A typical band structure of a bound-to-miniband multiple quantum wells and superlattices used in this experiment is shown in Figure 6.1.

To understand the miniband property and bound-to-miniband transition spectra, a corresponding calculation of energy states and transmission coefficient have been performed for the multiple layer $In_{0.52}Al_{0.48}As/In_{0.53}Ga_{0.47}As$ MQW/superlattice structures by using a multi-layer transfer matrix method. In the calculation, we used $E_g = 0.76$ eV and $m^* = 0.042$ m_0 for $In_{0.53}Ga_{0.47}As$, while $E_g = 1.47$ eV, and $m^* = 0.075$ m_0 for $In_{0.52}Al_{0.48}As$. The conduction-band discontinuity is taken as $\Delta E_c = 500$ meV. For simplicity, nonparabolicity, and screening effect are not considered in the current calculation. From the calculation it is noticed that there exists clearly a wide and strongly degenerated miniband E_{SL} (Figure 6.2) in the quantum well by introducing the superlattice into the barriers. The central energy position of the first miniband is at $E_{SL_1} = 138$ meV, and the bandwidth of the first miniband at $T \sim 0$ K is about $2\Gamma = 36$ meV. The room temperature (T = 300 K) bandwidth

is estimated to be $2\Gamma = 58$ meV. The increased bandwidth of the miniband would give a broad IR absorption, which can significantly improve the net integrated intersubband absorption strength I_A. The peak absorption wavelength can be found from Figure 6.2 by using relation $\lambda_p = 1.24/(E_{SL_1} - E_{SEW_1} + E_{ex})$, where $E_{SL_1} = 138$ meV, $E_{SEW_1} = 33$ meV, and $E_{ex} = 10$ meV [7,38], it gives $\lambda_p = 10.78$ μm. One notices that there is small energy shifts in the quantum well between those with superlattice AlInAs/InGaAs barrier (solid line) and uniform bulk AlInAs barrier (dashed line) since the effective barrier heights for the two case are no longer same. However, a big difference may lie in the large charge transmission probability exhibited by the resonant tunneling miniband (more than twenty orders of magnitude larger over the bulk barrier), indicating the miniband is an efficient charge transport channel.

The $In_{0.52}Al_{0.48}As/In_{0.53}Ga_{0.47}As$ MQW/SL layer structure for present study is grown on a lattice matched semi-insulating (100) InP substrate by using the molecular beam epitaxy (MBE) technique. A 1 μm thick GaAs buffer layer of 1.4×10^{18} cm^{-3} was first grown on a InP substrate, followed by the growth of a 20-period of enlarged $In_{0.53}Ga_{0.47}As$ quantum wells (EWs) with a well width of 110 Å and a dopant density of 1.4×10^{18} cm^{-3}. The barrier layer on each side of EW consists of a 6-period of undoped $In_{0.52}Al_{0.48}As$ (30 Å)/5-period of $In_{0.53}Ga_{0.47}As$ (46 Å) superlattice layers which were grown alternatively with the GaAs quantum wells (Figure 6.3). Finally, an n^+-GaAs cap layer of 0.3 μm thick and dopant density of 1.4×10^{18} cm^{-3} is grown on top of the MQW/SL layer structure.

The infrared absorption of the sample was measured at room temperature using a Perkin-Elmer Fourier transform infrared spectrometer. Since the intersubband resonance is expected to vanish at normal incidence (the selection rule requires a component of the incident electric field normal to the quantum well interfaces), the sample is oriented at the Brewster's angle ($\theta \sim 73°$) to maximize the intersubband absorption under surface illumination. Figure 6.4 shows the result of a room temperature

absorption spectrum measurement. The peak absorbance A = $-log_{10}$(transmission) is measured to be 36.5 mAbs , which corresponds to a transmission reduction of $\Delta T/T$ = 9 %. The absorption peak is at $\lambda = 10.73\mu m$, and the spectral full width at half-maximum (FWHM) of this transition is equal to 500 cm^{-1} (~ 62 meV), in very good agreement with our theoretical calculation. The small response at the shorter wavelength ($\lambda = 5.6 \ \mu m$) on the left of Figure 6.4 corresponds to the transition between the E_{SL_1} and E_{EW_3} as predicted in the Figure 6.2.

The intersubband absorption of this structure is due to the transitions between the first quasi-bound state (ground state E_{EW_1}) to the miniband state E_{SL_1} of the superlattice (SL) and the first excited state of enlarge quantum well (EW). Their energy levels are so closely packed together that they become a wide and highly-degenerated energy state—miniband. The total absorption is due to the contributions from all of the transitions between the first bound state and each sub-miniband state. Therefore, the integrated intersubband absorption strength I_A can be written [9] as

$$I_A = \int \int A(\lambda, E) dE d\lambda = \sum_{E_i} \sum_{E_f} n_s N \frac{e^2 h}{4\epsilon_0 m^* c} \frac{f}{n^2 \sqrt{n^2 + 1}} \qquad (6.1)$$

$$\simeq Q n_s N \frac{e^2 h}{4\epsilon_0 m^* c} \frac{f}{n^2 \sqrt{n^2 + 1}} \qquad (6.2)$$

The oscillator strength f is defined by

$$f = (4\pi m^* c/\hbar \lambda) < z >^2 \qquad (6.3)$$

where λ is the transition wavelength, $A(\lambda, E)$ is the spectral and energy dependence of intersubband absorbance, E_i and E_f denote the quantized energy levels for the initial and final states, $n_s = 1.54 \times 10^{12} \ cm^{-2}$ is the two-dimensional electron sheet density, $m = 0.042 m_o$ is the electron effective mass, N=20 is the number of enlarged quantum wells (EW), n = 3.6 is the refractive index of $In_{0.53}Ga_{0.47}As$ in the infrared range of interest, Q is the effective number of states within the miniband which contributes to the total intersubband absorption. Considering the fact that effective overlapping

and coupling of the electron wave function between the enlarged quantum well and the superlattice mainly occurs within the nearest regions (~ 120 Å) adjacent to either side of the enlarge quantum well, the effective number of miniband was found to be approximately $Q = 4.7$ for the present study. From Figure 6.4 we obtained a value of $I_A = 19.5$ Abs-cm^{-1} by integrating the area under the intersubband absorption spectrum. Substituting them into Eq. (6.2) and (6.3), we obtain $f = 0.73$ and $< z >$ $= 23.9$ Å which agreed reasonably well with our theoretical calculations of $f = 0.71$ and $< z > = 23.6$ Å.

6.4 <u>Results and Discussions</u>

The integrated absorption strength I_A is a useful parameter in characterizing the net intersubband absorption. However, the maximum value of I_A may vary greatly for different quantum well structures. For this reason, it may be worthwhile studying the parameter of integrated absorption strength I_A under the condition of bound-to-miniband transition. From Eq. (6.1) – (6.3) and Figures 6.2 and 6.4, the integrated absorption strength I_A is directly proportional to the two-dimension sheet density n_s ($\simeq n_d L_z$) and effective number Q of miniband. The large intersubband absorption spectra exhibited in the bound-to-miniband transition structure can be explained as follows: (1) For a given bandwidth and doping concentration n_d, a wider well allows a larger overlap of electron wave functions and dipole matrix element

$$< z > = < \phi_i z \phi_f > = L_z' \frac{16}{9\pi^2} \tag{6.4}$$

where L_z' is the effective enlarged quantum well width with a finite barrier V_0, and thus would give a higher peak absorption value; (2) an increased effective number Q of miniband for intersubband transitions would be helpful to enhance the infrared absorption efficiency and its peak value at a particular wavelength; (3) the large bandwidth of miniband would also be useful to give a broad bandwidth of absorption spectra, which, according to the definition [9], directly related to I_A by integrating

the area under the absorption spectra. So, a broad bandwidth of spectra would advantageous to obtain a large integrated absorption strength I_A as shown in the observations. However, it may be important to point out the different broadening mechanisms between the bound-to-continuum transition and bound-to-miniband transition are different in nature. The former is due to the broad virtually continuous state above the barrier potential height, and latter is mainly due to net contribution from a large number of narrow but high-degenerated quasi-bound states in the miniband formed by introducing the superlattice into the barrier regions. All the miniband states site deeply below the barrier potential and the corresponding noise due to thermionic emission out of wells can be greatly suppressed. Unlike the single bound-to-bound transition in which the value of Q is strictly limit to Q = 1, the bound-to-miniband transition structure can have a relatively wide the well width L_w, meanwhile its Q value can be made much greater than unit and the bandwidth can be made as broad as that in bound-to-continuum transition. Therefore, a large enhancement of intersubband absorption in the superlattice can be obtained. Figure 6.5 shows the calculated integrated absorption strength I_A of the bound-to-miniband transition as a comparison to the single bound-to-bound transition in the conventional quantum wells with uniform bulk barriers. As one expected, the I_A increases almost linearly with the well width L_z. With the help of the superlattice miniband, nearly five fold improvement in integrated absorption strength I_A has been achieved, which indicates a wide quantum well and a broad bandwidth would be helpful to obtain a large intersubband absorption. We also calculated the operational photon energy in the $In_{0.52}Al_{0.48}As/In_{0.53}Ga_{0.47}As$, taking the conduction band offset $\Delta E_c \simeq 500$ meV, and found that a broad range of photon absorption from 400 to 100 meV in photon energy $\hbar\omega$ can be covered, corresponding to the interest wavelength spectral from 3 to 12 μm, in this lattice-matched material system without having to switch to a different material, i.e. GaAs/AlGaAs system. These unique properties may be very useful

for realizing various multiple spectral (multi-color) detectors, and high quality image arrays, infrared lasers, and modulators.

6.5 <u>Conclusion</u>

In conclusion, we report the first observation of intersubband absorption of ground bound-to-miniband states transition in an InP lattice matched InAlAs/InGaAs multiple quantum wells/superlattice heterostructures. The peak transition wavelength and bandwidth are found to be $\lambda = 10.73\ \mu$m and $2\Gamma = 62$ meV in good agreement with the theoretical calculation. The dependence of the integrated absorption strength I_A on the well width and effective number of miniband was discussed. An integrated absorption strength $I_A = 19.5$ Abs-cm^{-1} for the present structure shows a significant enhancement over the conventional single bound-to-bound transition, confirming that a broad miniband and a wide quantum well are advantageous for a large intersubband absorption. By varying the well width the interesting spectral range $\lambda = 3$ - 12 μm can be covered, which may lead to novel infrared detectors and lasers.
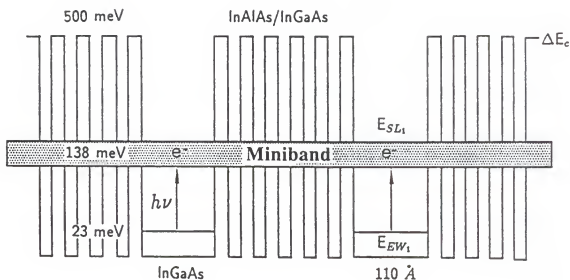
Figure 6.1 Schematic energy band diagram for intersubband transition from the localized ground bound state E_{EW_1} to the global miniband state E_{SL_1} (bound-to-miniband transition) in the enlarged InGaAs(110$\mathring{A}$) MQWs with short-period InAlAs(30$\mathring{A}$)/InGaAs(46$\mathring{A}$) superlattice barriers on InP substrate.
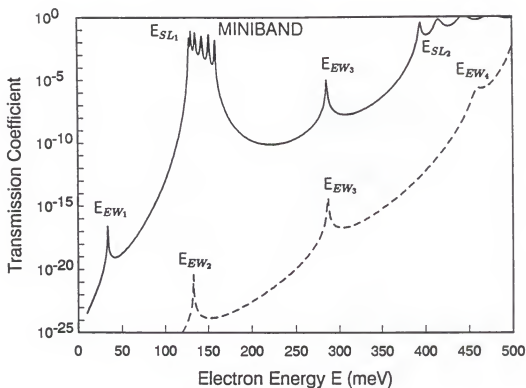
Figure 6.2 Calculated transmission coefficient T^*T vs. the electron potential energy E (meV) through the superlattice barrier. A broad and highly degenerated miniband is formed in the quantum well region with extremely large transmission probability (solid line), and nearly twenty orders of magnitude difference over that of the uniform bulk barrier (dashed line) was obtained.
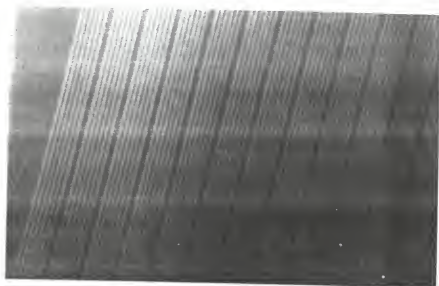
Figure 6.3 TEM micrograph of the InAlAs/InGaAs MQW/SL structure.
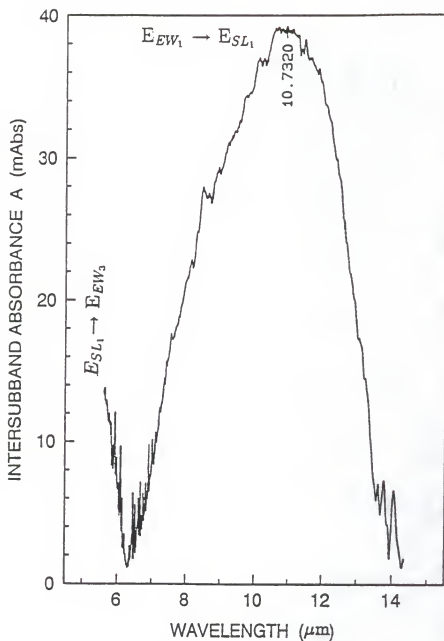
Figure 6.4 Measured intersubband absorbance at room temperature (T = 300 K) vs. infrared radiation wavelength by the Fourier transform infrared (FTIR) spectroscopy at the Brewster's angle.
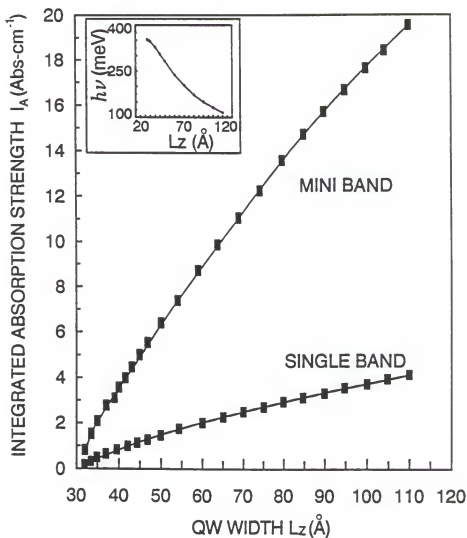
Figure 6.5 Calculated integrated absorption strength I_A for the superlattice mini-band reinforced bound-to-miniband transition and conventional single bound-to-bound transition.

CHAPTER 7

LOW DARK CURRENT STEP-BOUND-TO-MINIBAND TRANSITION InGaAs/GaAs/AlGaAs MULTIPLE QUANTUM WELL INFRARED DETECTORS

7.1 Introduction

The possibility of realizing novel high-speed quantum well devices such as lasers, photodetectors, and modulators has spurred extensive investigations on the intersubband absorption in quantum wells and superlattices [5-22]. A great deal of work has been reported on the lattice-matched GaAs/AlGaAs and InGaAs/InAlAs/InP quantum well systems. Recent studies [15,48] revealed that $8 - 12$ μm infrared detectors may be obtained by using a multiquantum well(MQW)/superlattice (SL) barrier structure and resonant tunneling mechanism. A significant improvement in intersubband absorption and thermionic emission property has been successfully demonstrated using GaAs/AlGaAs superlattice reinforced bound-to-miniband (BTM) transition structure. The replacement of bulk barrier region with a very short period superlattice barrier layer offers several new properties such as reduction of interface recombination, elimination of deep level related phenomena, realization of a new type of quantum photocurrent gain, and a significant enhancement of intersubband absorption [48].

7.2 Theory and Experiments

Here we describe an ultra-low dark current lightly-strained InGaAs/GaAs/AlGaAs QWIP's based on the step-bound-to-miniband (SBTM) transition, superlattice miniband resonant tunneling and coherent transport mechanism. As illustrated in Figure 7.1, the transition scheme of our QWIP's is from the localized bound ground

state in the enlarged $In_{0.07}Ga_{0.93}As$ quantum wells to the resonant-coupled miniband of $GaAs/Al_{0.4}Ga_{0.6}As$ superlattice (SL) barrier. This new structure created a potential 'step' in the superlattice barrier region to block the undesirable tunneling dark current from the heavily doped ground state E_{EW} in the quantum well. The physical parameters of the quantum wells and superlattices are chosen so that the ground bound state in the enlarged (EW) InGaAs well is pushed below the step barrier, and the first excited level E_{EW_1} of the quantum well is merged and lined up with the ground level of the miniband E_{SL} in the superlattice barrier layer to achieve a large oscillation strength f and intersubband absorption coefficient α. Since the superlattice has a relatively thin barrier, the photoexcited electrons can easily tunnel through the superlattice barrier layer and transport along the aligned miniband, which are then collected by the external ohmic contacts.

To characterize the SBTM transition we performed theoretical calculations of the energy states E_{EW}, E_{SL} and the transmission coefficient T^*T on our LWIP's by using the multiple-layer transfer matrix method, and the results are shown in Figure 7.2. It is noted that a broad and strongly degenerated miniband E_{SL} was formed inside the enlarged well by using the superlattice barrier structure. The ground state of the enlarged InGaAs well is confined much below the step barrier height so as to reduce the sequential tunneling and hopping currents. As a comparison, in the inset of Figure 7.2, we calculated the transmission coefficient of the superlattice for both the step-bound-to-miniband (SBTM) transition structure and the normal bound-to-miniband (BTM) transition structure without the potential step. Many orders of magnitude reduction in T^*T were observed in the present SBTM structure.

The SBTM detector structure was grown on a semi-insulating (S.I.) GaAs substrate by using the molecular beam epitaxy (MBE) technique. A 1 μm thick GaAs buffer layer of 1.4×10^{18} cm^{-3} was first grown on a S.I. GaAs substrate, followed by the growth of a 40-period of $In_{0.07}Ga_{0.93}As$ quantum wells with a well width of 106 Å

and a dopant density of 1.4×10^{18} cm^{-3}. The barrier layer on each side of the quantum well consists of a 5-period of undoped $Al_{0.4}Ga_{0.6}As$ (30 Å) /GaAs (59 Å) superlattice layers which were grown alternatively with the InGaAs quantum wells. Finally, an n^+-GaAs cap layer of 0.4 μm thick and dopant density of 1.4×10^{18} cm^{-3} was grown on top of the MQW/SL layer structure to facilitate ohmic contacts. An array of 200 $\times$ 200 μm^2 mesas were chemically etched down to n^+-GaAs buffer contact layer on the GaAs substrate. Finally, AuGe/Ni/Au ohmic contacts were evaporated onto the top and bottom of n^+-GaAs contact layers by using E-beam evaporation.

Device characterization was performed in a liquid-helium cryogenic dewar. An HP4140B semiconductor parameter analyzer was used to measure the dark current vs. voltage (I-V) curves. Under dark conditions, electrons can transfer out of the quantum wells and produce the observed current mainly via two mechanisms. One is attributed to the thermionic emission out of the quantum wells, which is the dominant current component at higher temperatures (i.e., for $T \geq 77$ K). The other is the thermally generated carriers tunneling through the superlattice miniband. In the present SBTM transition structure, we created a levitated potential step in the superlattice to block much of the tunneling current component due to electron tunneling from the heavily populated ground state at low temperatures. We also chose a high value of 'Al' composition, $x = 0.4$, which gave rise to a barrier potential as high as $\Delta E_c \simeq 388$ meV ($\sim 65\% \Delta E_g$), to suppress the thermionic emission out of the quantum wells. Figure 7.3 shows the measured dark I-V curves for temperatures between 35 and 92 K. Substantial reduction in device dark current was achieved in the present step-potential reinforced InGaAs multiquantum well/GaAs/AlGaAs superlattice barrier structure.

To identify the origins of the dark currents flow in the detector we performed the numerical calculation of the dark currents using the expression [14,21]

$$I_D = \frac{4\pi q A v(\mathcal{E}) m^* kT}{h^2 L} \int_0^\infty |T(E,\mathcal{E})|^2 \{ln[1 + e^{-(E-E_f)/kT}] - ln[1 + e^{-(E-qV-E_f)/kT}]\} dE; \tag{7.1}$$

where $v(\mathcal{E})$ is the electron velocity in GaAs which is given by [49]

$$v(\mathcal{E}) = \frac{\mu\mathcal{E} + v_s(\mathcal{E}/\mathcal{E}_0)^4}{1 + (\mathcal{E}/\mathcal{E}_0)^4} \tag{7.2}$$

where q is the electron charge, A is the device area, m^* the electron effective mass, L is the multiquantum well period, E_f is the Fermi level, $\mathcal{E}_0$ is the critical field which is equal to 4×10^3 V/cm for GaAs. As previously described [43], the parameter $|T(E,\mathcal{E})|^2$ is the field-dependent transmission coefficient which can be calculated by using the multi-layer matrix method, assuming the potential energy variation of $V(x) = V_0 + q\mathcal{E}x$. The calculated current values are in good agreement with the observed results, which shows that the levitated step potential barrier is indeed very effective in suppressing the device dark current. Another interesting result observed in this SBTM LWIP's (as shown in Figure 7.3) is that the negative resistance exhibited by the sequential resonant tunneling through an expanding high-field superlattice domain [50] at a low temperature. A detailed study of the device conductance was also performed at T = 77 K (Figure 7.4). The high-frequency oscillations of the measured conductance confirms the existence of the resonant tunneling (RT) and negative differential resistance (NDR).

Measurement of the intersubband absorption for the present detector was performed at 300 K using a Fourier transform infrared (FTIR) spectroscopy. Figure 7.5 shows the room temperature absorption spectra at the Brewster's angle ($\theta_B = 73°$). The measured peak absorbance A = -$\log_{10}$ [transmission] was found to be about 40 mAbs. The absorption peak is centered at 11.4 μm. The full width at half-maximum (FWHM) of the absorption peak is about 220 cm^{-1}. To determine the spectral responsivity, the edge of the sample was polished into $50°$ to facilitate light illumination.

The photocurrent was measured using a CVI Laser Digikrom 240 monochromator and an ORIEL ceramic element infrared source. The responsivity $R_\lambda = 0.38$ A/W was obtained at $V_b = 5$ V and T = 77 K. Figure 7.6 shows the normalized responsivity versus wavelength measured at 77 K. From the measured responsivity and dark current, we can calculate the detectivity D^* of the detector using the relation

$$D_\lambda^* = R_\lambda (A\Delta f)^{1/2} / (4qI_d G\Delta f)^{1/2} \qquad (7.3)$$

where A $= 4 \times 10^{-4}$ cm^2 is the effective area of the detector, G is the optical gain which is taken as 0.5^4. At $V_b = 5$ V, we found that values of the peak detectivity at $\lambda = 10.5$ μm are $D^* = 0.81 \times 10^{10}$ and 2.1×10^{10} cm$\sqrt{Hz}$/W for T = 77 and 63 K, respectively.

7.3 Advantages of Step-Bound-to-Miniband Transition Structure

There are many unique features about the newly developed InGaAs/GaAs/AlGaAs SBMT MQW IR detector. Some of them are listed as follows:

- **High Operation Temperature and Low Dark Current:** Dark current is a key device parameter for the background limited QWIPs, especially for temperatures T $\geq$ 77 K. For a conventional bound-to-continuum transition QWIP, under dark condition, electrons can transfer out of the quantum wells and produce the observed dark current mainly via two mechanisms. One is the thermionic emission out of the quantum wells, and the other is the carrier tunneling through the superlattice along the miniband. Based on our calculation, it can be shown that the former mechanism is the dominant component of the dark current at low bias and at higher temperatures. With the new bound-to-miniband device structure and the adoption of a much larger barrier height V_0, the E_3 and other closely spaced higher continuum states could be lifted far away from E_2 and miniband of the SL. Meanwhile the bound states of the quantum wells

are deeply "positioned" inside the superlattice and far from the quasi three-dimensional continuum states above the barrier. Due to relatively large barrier height, the thermionic emission current out of the quantum wells is expected to be effectively suppressed. The introduction of a step bulk barrier in the new step-bound-to-miniband transition (SBMT) structure allows the ground state level of the enlarged quantum well to be located below the step bulk barrier in the superlattice, and the tunneling current can also be further suppressed. Therefore, significant reduction in the detector dark current can be expected from this new structure.

• **Dual-mode Operation:** Low bias operation is always preferred in many infrared applications. Due to the strongly coupled coherent states—miniband transport in the SBMT structure, a large portion of the electron wave functions in the superlattice region is overlapped and the discrete quantum levels of the different superlattice layers are so closely packed, a strongly degenerate miniband is formed in the superlattice barrier region. There exist large coupling effects among these states. In other words, the excited electrons in the miniband are co-governed and shared by different quantum wells in the superlattice region, and the resonant tunneling can easily take place along the miniband even with a small perturbation or an external applied electric field. It is interesting to note that we have observed a relatively large photocurrent in such a detector even at zero bias. Therefore, the low bias operation, or zero bias condition (dual-mode operation) could be realized in the proposed SBMT MQW IR detector using a short period of superlattice barrier.

• **High Optical Gain:** A large optical gain can be achieved in the proposed SBMT MQW IR detector. Unlike the conventional GaAs QWIP's, the carrier transport in this SBMT MQW IR detector structure is via the lowest miniband—the ground state of the SL. The photocarriers in the ground state

miniband have a longer lifetime than that in the higher order minibands, and the re-capture rate by the quantum wells is also much lower in the ground level miniband. With a proper design, it is possible to realize a higher photocurrent gain, given by $G = \tau_e/t_{tr}$, in the QWIP based on the miniband transport and effective mass filtering effect [5], where τ_e is the electron lifetime in the superlattice and t_{tr} is the electron transit time. Since the tunneling probability increases exponentially with the reduction of barrier width in the superlattice and the tunneling time decreases with the reduction of the barrier width, by adjusting the superlattice structure parameters, an optical gain much greater than unity can be obtained in this proposed IR detector.

- **High Speed:** Due to the effective mass filtering effect in the step-bound-to-miniband transition (SBMT) structure, the holes are relatively confined in the superlattice region, and the electron transport is via the lowest miniband—the ground state of the SL. The resonant tunneling time along the aligned miniband can be very short and hence a high response speed at 10μm wavelength can be expected in this detector.

- **Adjustable Spectral bandwidth:** In our proposed SBMT MQW IR detector structure, the bandwidth of spectral response of the detector is mainly determined by the aligned coherent miniband, which is a strong function of the superlattice barrier width. A thin barrier will give a broad photoresponse bandwidth, and a thick barrier will result in a very narrow photoresponse bandwidth. Furthermore, with a hybrid combination of varying the widths of the superlattice barrier and the quantum well, we can select an optimum barrier width which will enable us to cover a broad uniform spectral bandwidth from 8 to 12 μm with high quantum efficiency and high responsivity.

7.4 <u>Conclusion</u>

In conclusion, we have demonstrated a new step-bound-to-miniband (SBTM) transition LWIP's using a lightly-strained InGaAs multiquantum well and a GaAs/AlGaAs superlattice barrier layer structure and resonant tunneling mechanisms. The new structure provided a levitated potential step in the superlattice barrier to block much of the tunneling current component from the heavily populated ground state in the quantum wells, which resulted in a significant reduction of the device dark current. The peak detectivity was found to be $D^* = 2.1 \times 10^{10} cm\sqrt{Hz}/W$ at $\lambda = 10.5$ μm and T = 63 K. With high detectivity and uniformity, this new SBTM LWIP can be used for a wide variety of long wavelength (e.g., 8 – 12 μm) infrared applications.
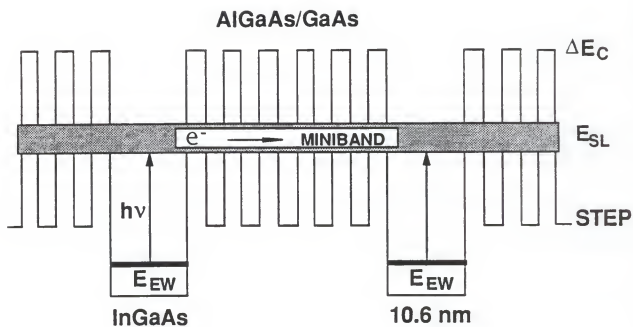
Figure 7.1 The schematic energy band diagram for the step-bound-to-miniband (SBTM) transition in a new LWIP's structure by using lightly strained InGaAs (106 $\mathring{A}$) material. A potential 'step' is created in the GaAs/AlGaAs superlattice barrier layer to suppress the tunneling current from the heavily populated ground state in the InGaAs quantum well.
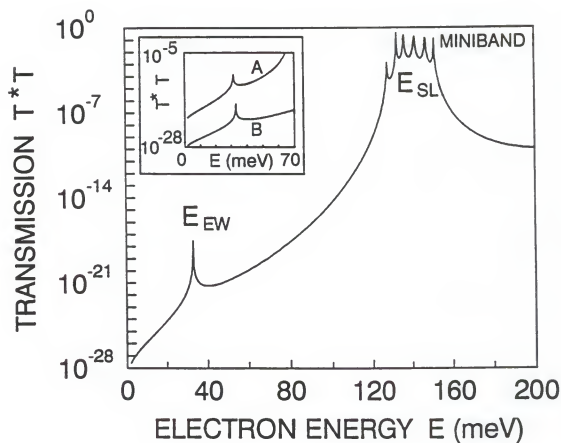
Figure 7.2 The calculated quantized energy states and transmission coefficient T^*T for the present SBTM transition structure. Inset: The calculated T^*T for a SBTM (curve B) and a BTM (curve A) LWIP's.
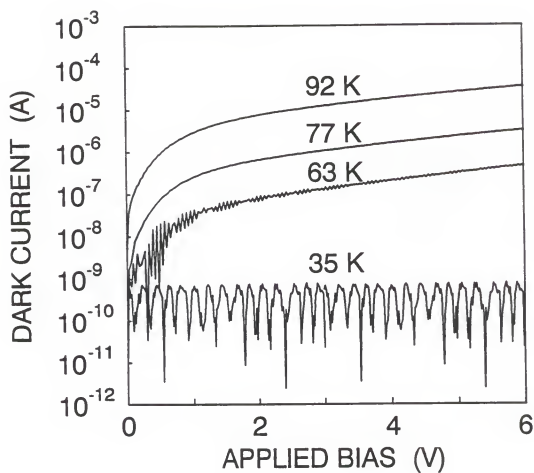
Figure 7.3 Measured dark current vs. applied bias for a SBTM LWIP's for $35 < T < 92\ K$. Note that the dark current is dominated by thermionic emission for $T \geq 77K$ and by sequential tunneling and hopping for $T \leq 50$ K.
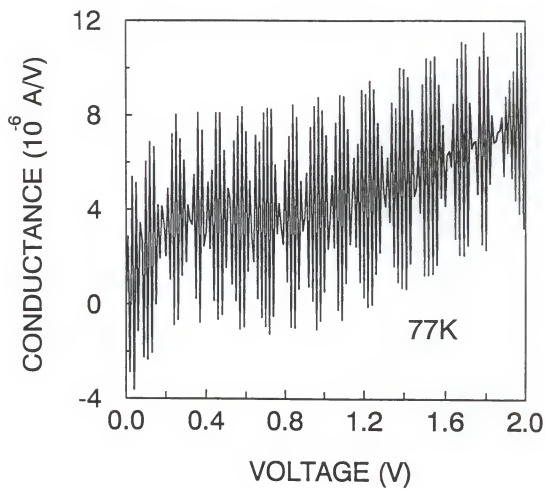
Figure 7.4 A detailed study of negative differential conductance and miniband transport.
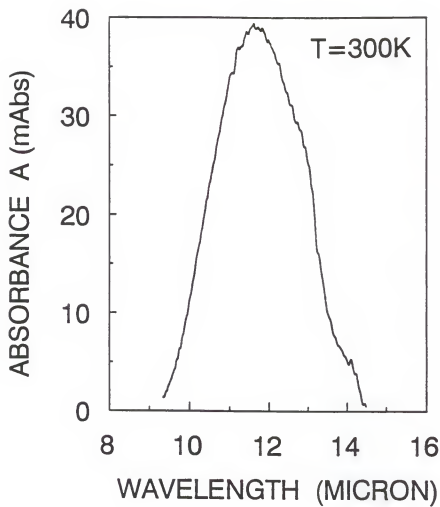
Figure 7.5 Measured room temperature (T = 300 K) intersubband absorbance versus wavelength for the SBTM LWIP's by FTIR spectroscopy at Brewster's angle.
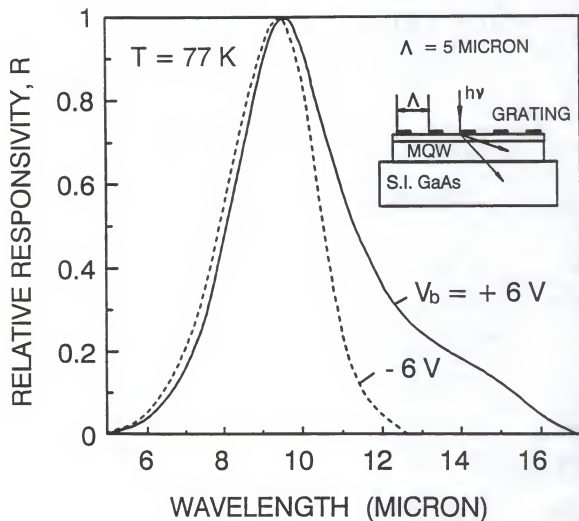
Figure 7.6 Relative responsivity versus wavelength for a SBTM LWIP's measured at 77 K. A broad spectral sensing range is obtained. As noticed by changing the bias direction, the miniband reinforced infrared detector has the capability of tunable band width.

CHAPTER 8
COUPLING EFFICIENCY VERSUS GRATING PERIODICITY
IN NORMAL INCIDENT GaAs/AlGaAs MULTIPLE
QUANTUM WELL INFRARED DETECTORS

8.1 Introduction

There has been a considerable interest in edge illuminated long wavelength quantum well infrared photodetectors (QWIPs) and modulators sensitive in the atmospheric window of 8 - 12 μm [10-61]. Several studies have been reported on the phase modulated reflection metal grating coupled QWIPs and arrays [54-56] using a backside surface illumination. Recently, we have demonstrated an amplitude modulated metal grating coupled AlGaAs/GaAs QWIP with front normal illumination [15,57]. A thin (0.1 μm) metal grating contact structure is formed on the detector surface to serve both as an effective infrared light coupler and as a top ohmic contact. The main advantage of using a metal grating structure is that the vector of electric field on the metal grating is always perpendicular to the metal surface which is essential for enhancing the intersubband absorption in the quantum well detectors. Using a 5 μm grating periodicity, a peak detectivity $D^* = 1.6 \times 10^{10}$ cm$\sqrt{Hz}$/W has been obtained at $\lambda_p = 8.9$ μm and T = 77 K with front side normal illumination. This simple but extremely uniformed planar grating coupler structure is indeed very favorable for use in the large area infrared detector arrays and image sensors.

It is well known that electric dipole matrix element existing between the subbands of a quantum well is relatively large. However, since only the component of IR radiation with electric field $\vec{\mathcal{E}}_\perp$ vector perpendicular to the quantum well layers will give rise to intersubband transition in the quantum wells, no intersubband infrared absorption in the quantum wells is expected in the ordinarily bare surface at

72

normal incidence. Even tilted 73° at the Brewster's angle, due to the large refractive index n = 3.3 and the anisotropic character of the absorption, only a small fraction, $\cos^2(\theta_B)/\sin(\theta_B) = 9\%$, of the incident light can be absorbed. In fact, the practical net absorption is only about 4%. For a large and uniformed surface illumination, a textured diffraction surface, or metal grating, is needed to induce the perpendicular electric field component for intersubband resonance [58].

The key grating parameter of the metal grating structure which controls the coupling quantum efficiency of the normal incident IR illumination is the grating periodicity. The IR light coupling efficiency is strongly dependent on the grating periodicity for a given wavelength. Amplitudes of the transmitted waves and the diffracted angles could vary significantly with a change of the grating periodicity. Thus, the performance of a quantum well infrared detector can be quite different when different grating parameters are used for top contacts in the detector. The objective of this paper is to conduct a theoretical and experimental study of the relationship between the coupling quantum efficiency and the grating periodicity in a normal incident GaAs/AlGaAs quantum well IR detector at $8 - 10$ μm wavelength. The results of this study may help us to further improve the performance of various metal grating coupled multi-quantum well infrared (IR) detectors and arrays.

8.2 Sample Preparation

The intersubband transition quantum well IR detector structure was grown by using the molecular beam epitaxy (MBE) technique. The growth sequence for the GaAs/AlGaAs multiquantum well IR detector structure sample started with a 1.0 μm buffer layer of n-GaAs (1.4×10^{18} cm^{-3}) grown on a semi-insulating (S.I.) GaAs substrate. This was followed by the growth of a 40-period of multiquantum wells with alternating doped (n = 1.4×10^{18} cm^{-3}) GaAs quantum well layers of 39 $\mathring{A}$ and undoped $Al_{0.25}Ga_{0.75}As$ barrier layers of 490 $\mathring{A}$. Finally, an n-GaAs cap layer of 0.4 μm thick and dopant density of 2.0×10^{18} cm^{-3} was grown on top of the multiquantum

well layer structure. To facilitate the photocurrent measurements, the detectors are made into arrays of chemically etched mesas down to the highly doped buffer layer with an effective area of $200 \times 200 \ \mu m^2$. The bottom ohmic contact was formed by evaporating Au-Ge/Ni/Au on the buffer layer.

8.3 Theory

We assume that the metal strips in the grating contact structure (Figure 8.1) have a large conductivity σ and a negligible thickness ($h \rightarrow 0$). The metal is equivalent to a lossy dielectric with relative permittivity $\epsilon = 1 + i\sigma/\epsilon_0\omega$. When an infrared light is shined normally upon the grating surface, the corresponding transmission magnetic field in the GaAs/AlGaAs quantum well region can be expressed by [59]

$$H_t(y, z) = T_0 e^{ikz} + \sum_{m=1}^{\infty} T_m cos(8m\pi y/\Lambda)e^{i\Gamma_m z} \tag{8.1}$$

where T_0 is the zeroth-order transmission coefficient, Γ_m is the Gamma function of order m, and T_m ($m = 1, 2, \cdots$) is the high order transmitted wave amplitudes which can be written as

$$T_{2n} = (-1)^n \frac{K_+(k)K_+(\Gamma_{2n})}{2\Gamma_{2n}(k + \Gamma_{2n})}t, \qquad n = 1, 2, \cdots \tag{8.2}$$

$$T_{2n-1} = (-1)^n \frac{K_+(k)(k + \Gamma_{2n-1})}{(2n-1)\pi\Gamma_{2n-1}K_+(\Gamma_{2n-1})}t, \qquad n = 1, 2, \cdots \tag{8.3}$$

where t is the transmission coefficient at the GaAs surface and K_+ is given by

$$K_+^{-1} = (w + k)^{-1} \prod_{n=1}^{\infty} \frac{w + \Gamma_{2n-1}}{w + \Gamma_{2n}} \frac{2n}{2n - 1} \tag{8.4}$$

In Figure 8.2, the theoretical calculations of transmitted powers versus normalized grating periodicity $n_1\Lambda/\lambda$ are presented for each excited diffractive mode, where n_1 is the refractive index of GaAs. The grating coupling equation for the forward-diffracted (transmitted) waves can be written as [60]

$$n_1 sin\theta_t^{(m)} = n_0 sin\theta_i - \frac{m\lambda}{\Lambda}sin\phi \tag{8.5}$$

where n_0 and n_1 denote the optical refractive indices of layers above and beneath the grating layer, respectively, and are given by $n_0 = \sqrt{\epsilon_0}$ and $n_1 = \sqrt{\epsilon_1}$. The cutoff periodicity Λ_c for the mth diffracted mode for a given incident angle θ can be estimated by using the relation

$$\Lambda_c = \left| \frac{\pm m\lambda}{\pm sin\theta_i - (\epsilon_1)^{1/2}} \right| \qquad m = 0, 1, 2, \cdots \tag{8.6}$$

where λ is the incident wavelength, ϵ_1 is the dielectric constant of GaAs which is equal to 10.7. Substituting into Eq. (8.6), the first three cutoff periodicities for the incident wavelength of 9.8 μm under normal incidence were found to be roughly equal to 3, 6, and 9 μm, respectively.

The angle dependence of the intersubband optical absorption coefficient α as a function of the mth diffracted angle θ_t^m in the multiple quantum well/ superlattice layer can be found by using the relation [61]

$$\alpha[\theta_t^{(m)}] = \frac{e\omega\mu c m^* I}{n_3 L'_{EW} \pi \hbar^2} \sin^2 \theta_t^{(m)} \tag{8.7}$$

where m^* is the electron effective mass for GaAs; μ is the permeability; L'_{EW} is the effective width of the infinity potential quantum well which is slightly larger than the finite potential well width; c is the speed of light in free space; I is the relative transition probability between the ground state and the miniband state which is given by

$$I = \int_0^\infty dE \frac{\langle z \rangle^2 (f_1 - f_2) \Gamma_{12}}{(E_2 - E_1 - E_{xch} - \hbar\omega)^2 + (\Gamma_{12})^2} \tag{8.8}$$

where $2\Gamma_{12}$ is the intersubband full width at half maximum (FWHM); $\langle z \rangle$ is the dipole matrix element; E_{xch} is the energy shift mainly due to exchange energy correction and depolarization effect in a highly doped quantum well [37,38,62]; $f_{1,2}$ is the Fermi function given as $f_{1,2} = [1 - exp(E_{1,2} - E_f)/kT]^{-1}$; E_f is the Fermi level; k is the Boltzmann constant; E_1 and E_2 are the energy eigenvalues of the subbands in the quantum well, which can be found by using the transfer matrix method. For our present structure, the parameters used in the calculation are: $E_1 = 96$ meV, $E_2 = $

210 meV, $E_{xch} \simeq 10$ meV, $E_f = 102.8$ meV, $n_3 = 3.3$, $m^* = 0.0665$ m_0, $L'_{EW} = 62$ Å, $2\Gamma_{12} = 20$ meV, and T = 77 K. Figure 8.2 shows the calculated angle dependence of the intersubband absorption coefficient $\alpha(\lambda, \theta_t)$ under diffracted angles $\theta_t = 90°$, $50°$, and $25°$, respectively. The photocurrent responsivity R_λ of the multiquantum well IR detectors can be expressed as

$$R_\lambda(\Lambda) = \eta(\Lambda) \cdot \frac{e\lambda}{hc} G, \qquad (A/W) \qquad (8.9)$$

where e is the electronic charge; G is the photoconductive gain; η is the detector's quantum efficiency which can be determined by using the expression

$$\eta(\Lambda) = \frac{1}{2} \sum_m \frac{\Gamma_m |T_m(\Lambda)|^2}{2k} \{1 - e^{-\alpha[\theta_t^{(m)}(\Lambda)]L}\} \qquad (8.10)$$

where L is the total length of the superlattice absorption region. A factor of $1/2$ in front of the summation above is included to account for the reduction of an un-polarized light source. By substituting Eqs. (8.2), (8.3), and (8.7) into (8.10), we obtain a normal incident single pass quantum efficiency of 11 %, 1.4 %, and 8.3% for the samples with grating periodicities of 5, 7, and 10 μm, respectively, at the peak wavelength $\lambda_p = 9.8$ μm and operating temperature T = 77 K. When an incident light is polarized along the direction perpendicular to the grating strips, the quantum efficiency will increase by a fact of two, which yields $\eta = 22$ % for the 5 μm grating coupled IR detector under the front side illumination.

8.4 Results and Discussions

A set of metal grating contacts with different periodicity lengths of 1.1, 3.2, 5, 7, and 10 μm were deposited onto the n^+-type GaAs cap layer by using electron beam evaporation to form the top ohmic contacts. Figure 8.3 shows one of the fabri-cated planar grating patterns, which has a grating periodicity equal to 5 μm. Device characterization was carried out in a close-cycled liquid-helium cryogenic dewar. The photocurrent was measured as a function of temperature, wavelength, and applied

bias, using a CVI Laser Digikrom 240 monochromator and an ORIEL ceramic element infrared source. Due to the very large device resistance and small values of dark current I_d present in the device , the short-circuit measurements were used to determine the photocurrent I_{ph} [15]. Since the metal surface only has a normal electric field vector, the x-component of the IR radiation, $\vec{\mathcal{E}_x}$, is zero in the highly conductive regime. Therefore, the IR beam is spatially modulated in the near field of the grating, and has a z- component of the electric field $\vec{\mathcal{E}_z}$ which can induce perpendicular excitation of intersubband resonance. It is noted that the optimal grating periodicity is obtained for a grating periodicity which is neither too small nor too close to the incident IR radiation wavelength. We have found that a periodicity of $\Lambda = 5 \ \mu m$ gives the best front coupling efficiency, followed by 10, 7, 3.2, and 1.1μm. This is illustrated in Figure 8.4 for the grating enhanced intersubband excitation at normal incidence. The peak wavelength was around 9.8 μm with its cutoff wavelength around 10.8 μm at T = 77 K. The experiments are in good agreement with our calculations.

The backside illumination experiment was also conducted by shining the infrared light through the S.I. GaAs substrate surface. The results revealed that the corresponding responsivities for the tested samples are quite similar to those of the front illuminated samples for most of the grating periodicities. The results showed, even though it yielded a very close photoresponse as what the 5 μm grating would give, the 7 μm grating periodicity gave the best coupling efficiency under the backside illumination. It is not surprising to see such a difference since the backside illumination is based on the internal reflection coupling mode inside the GaAs semiconductor (n_s) layer, in stead of the front normal air/semiconductor ((n_0/n_s) transmission. A similar calculation can be performed by replacing the transmission coefficient T_m with the reflection coefficient R_m (m = 1,2 $\cdots$) and substituting into Eqs. (8.5) - (8.10). It can be shown that the previous theory is still valid.

The results further suggest that the high conducting strip grating can be used effectively not only as an efficient transmission coupler for front side normal illumination but also as a reflection coupler for the backside illumination. This new improvement will provide an additional value and structural option for the infrared application and industrial manufacturing.

We performed the angle dependence measurement of the photocurrent in our grating coupled GaAs/AlGaAs quantum well IR detectors. Figure 8.5 shows the relative photoresponse as a functions of the incident angle θ_i for the detector using a 5 μm grating coupler. Similar measurement was also performed for the device with a 7 μm grating coupler, and the result is shown in Figure 8.6. The relatively slow variation with respect to the incident angle indicates that there are more than one higher order modes passing through the grating slit and propagating into the quantum well layers, or the first transmitted TM mode is far from the cutoff frequency. The relative insensitiveness to the incident angle is a desirable feature for the large field of view image sensor arrays.

8.5 Unique Features of Planar Metal Gratings

It is important to point out some of unique features by using the planar metal grating couplers for long wavelength quantum well infrared detection. They are described as follows:

(1) Excellent uniformity for grating coupler by E-beam evaporation. The arrays pixel uniformity is an important figure of merit for evaluating good image properties of focal plane arrays (FPAs). Without use of chemical etching, the inhomogeneous proportion of chemical contents, and the influence of temperature gradient and fluctuation, a precisely controlled and well established E-beam evaporation technique is definitely much more advantageous to give high uniformity of grating film pattern over the entire detector arrays than any

other chemically etched methods. We also expect that due to the high uniformity of the MBE growth of GaAs/AlGaAs quantum well/superlattice structure, an extremely high uniformity can be achieved with metal grating coupled GaAs/AlGaAs MQW IR detector arrays, which is considerably better than any of the conventional HgCdTe detector arrays. Therefore, high quality imaging can be readily achieved in the proposed SBMT MQW IR detector arrays.

(2) High yield and low cost. The planar AuGe grating film pattern can be readily deposited onto the detector surface by using E-beam evaporation. The film thickness of the grating coupler is equal or less than 0.12 μm. Unlike most conventional nonplanar or saw-tooth shape etched gratings, the metal grating film coupler does not require chemical etching which is unstable and more difficult to control. The E-beam evaporation is much more precise and easy to control. In contrast to the non-planar grating pattern etchings, our planar metal grating approach does not require very thick metal film, which is usually much larger than the active superlattice layer. As a result, it can significantly cut down the expensive molecular beam epitaxy (MBE) growth time. Furthermore, the metal grating itself can also be used as one of the ohmic contacts for the detector output, and thus coupler and ohmic contact can be made simultaneously. With the advantages cited above, high yield and low cost production of the GaAs/AlGaAs MQW IR detector arrays can be expected for FPA IR sensor system applications.

(3) Suitable for large hybrid and monolithic integration. Due to the simple and uniform planar grating structure and the ultra thin metal grating film used, the metal grating coupled SBMT MQW IR detector arrays are superior and favorable for the monolithic integrated FPA technology for staring IR sensor system applications.

(4) Good for both front and backside illuminations. Since we use the strip-metal grating structure, both the top front and backside illuminations are allowed on the array chip. It provides a new option for FPA sensor packaging. Top illumination would be advantageous for monolithic integration with GaAs signal processing electronics, while backside illumination is desirable for applications where the detector array chip is flipped over and stacked onto silicon imaging and signal readout chips. Therefore, a large hybrid and even complete integration of the arrays and pre-amplifier and signal processing circuits for infrared FPA can be achieved on a single chip with a metal grating coupled GaAs/AlGaAs SBTM MQW IR detector structure.

(5) Elimination of the undesirable crosstalk. Elimination of crosstalk is a key factor for producing high quality IR image sensors. With the top planar grating coupling arrangement, only the mesa region beneath the grating film could have the intersubband transition and absorption due to the regular surface perturbation (grating). The incident light passes through each mesa (pixel) structure only once at a time and does not enter the other mesas. There is no interference among the different mesas (pixels). The light path and relative position are well defined. Therefore, the relative shape and light intensity distribution and quality of the images can be well maintained in the infrared image sensing arrays and staring systems using the proposed grating coupled MQW IR detectors.

8.6 Conclusion

In conclusion, we have performed a detailed theoretical and experimental study of the effect of grating periodicity on the coupling quantum efficiency in the normal incident planar metal grating coupled GaAs/AlGaAs quantum well IR detectors in the 8 - 12 μm wavelengths. The dependence of the responsivity and quantum efficiency on the grating periodicity for these IR detectors have been investigated. The results

show that the optimal grating periodicity for these MQW IR detectors is about 5 μm for the front side normal illumination and 7 μm for the backside illumination case. A single pass quantum efficiency as high as 11 % has been achieved for the 5 μm grating coupled GaAs/AlGaAs MQW infrared detector, which is in good agreement with our theoretical prediction. The advantages of high uniformity, low cost, high yield, and elimination of cross-talk offered by using planar metal grating couplers are essential for developing high quality GaAs/AlGaAs MQW IR arrays and image sensors .
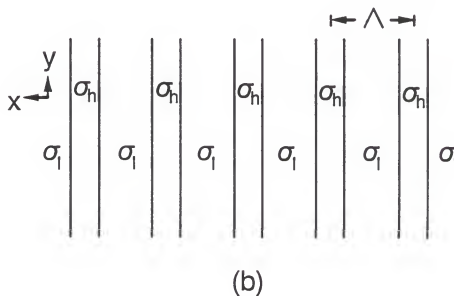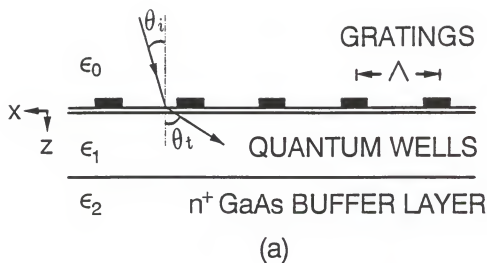
Figure 8.1 Configuration of a front incidence strip metal grating coupler on a GaAs/AlGaAs multiple quantum well IR detector structure: (a) side view showing the grating periodicity Λ and diffraction angle θ_t, (b) top view of the grating modulation planes with with alternated high σ_h and low σ_l conductivity regions.
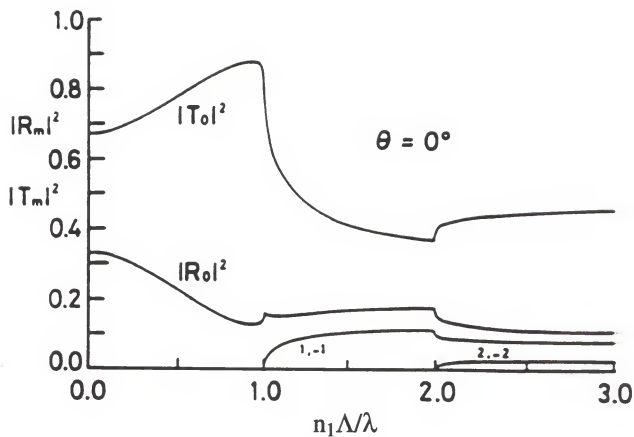
Figure 8.2 The relative transmitted powers versus normalized grating periodicity $n_1\Lambda/\lambda$ for a strip-metal grating on the GaAs wafer, where n_1 is the refractive index of GaAs.
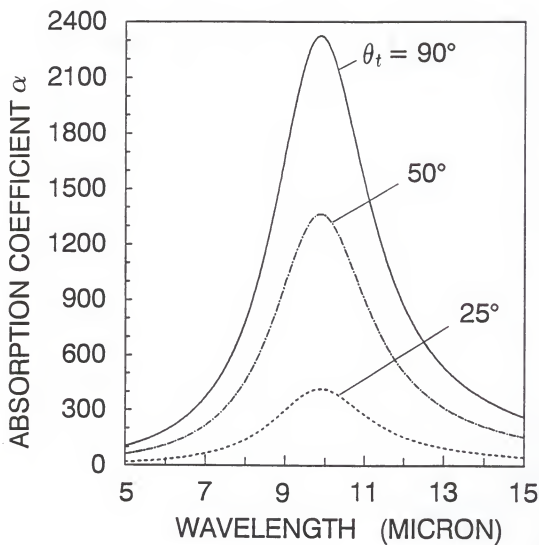
Figure 8.2 Calculated diffraction angle dependence of intersubband absorption $\alpha[\theta_t]\,(cm^{-1})$ in the multiple quantum well layer.
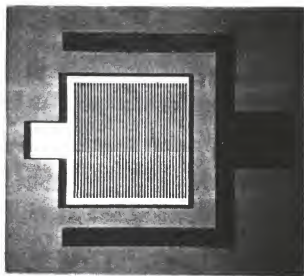
Figure 8.3 Top view of the fabricated AuGe/Ni/Au metal grating pattern with a 5 μm periodicity and a $200 \times 200 \ \mu m^2$ area for front side light coupling and ohmic contact.
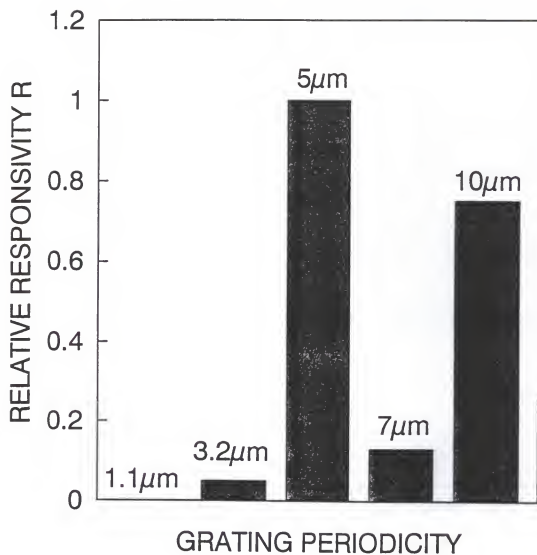
Figure 8.4 Measured relative responsivity versus grating periodicity for five different grating periodicities (1.1, 3.2, 5, 7, and 10 μm, respectively) at T = 77 K.
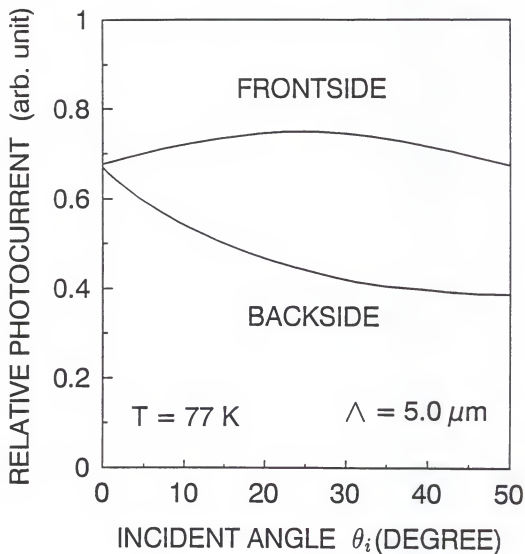
Figure 8.5 Relative photocurrent I_{ph} versus incident angle θ_i of IR radiations for the front side and backside illumination, using a 5 μm grating periodicity.
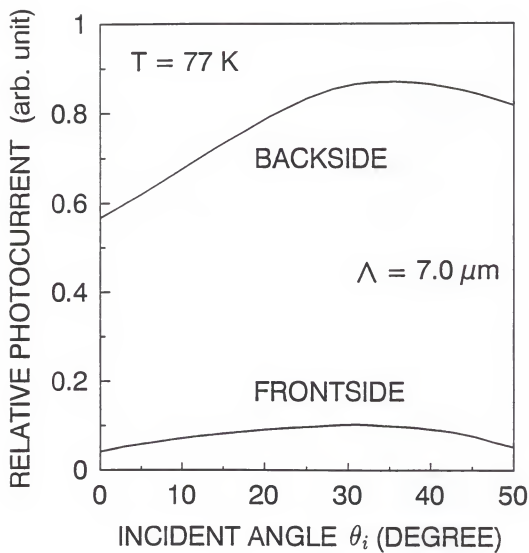
Figure 8.6 Relative photocurrent I_{ph} versus incident angle θ_i of IR radiations for the front side and backside illumination, using a 7 μm grating periodicity.

CHAPTER 9
NOVEL NORMAL INCIDENCE INDIRECT TYPE-II
AlAs/AlGaAs QUANTUM WELL INFRARED DETECTOR
GROWN ON [110] GaAs SUBSTRATE

9.1 Introduction

Most work on quantum well infrared photodetectors (QWIPs) has been focused on type-I direct and conventional Γ-band GaAs quantum well structures [11-15,42-47] grown on GaAs [001] direction, in which the shapes of constant energy surfaces are isotropic with spherical symmetry. In this type of structure, due to the selection rule [9], only the component of IR radiation with electric field $\vec{\mathcal{E}}_\perp$ vector perpendicular to the quantum well layers will give rise to intersubband transition in the quantum wells. No intersubband infrared absorption in the quantum wells is expected in the ordinarily bare surface at normal incidence. In general, a grating coupler [54,55], or 45 ° incidence [13] is required to induce the perpendicular electric field component for intersubband resonance. Recently, we have successfully demonstrated high performance quantum well infrared detectors by using a top surface strip metal-grating coupler for normal incidence. We have also found that the infrared coupling efficiency is strongly grating-period dependence as discussed in previous chapter.

Motivated by the possibility of realizing normal incidence quantum well infrared detectors without using the complex grating structures, we conducted a study of using type-II indirect III-V quantum well heterostructures for long wavelength infrared detectors. In such a system the conduction-band minimum is at the X point of the Brillouin zone (BZ). The constant energy surface will also undergo change from a typical sphere at the zone center of direct (i.e. GaAs) to off-center ellipsoids of

indirect (i.e. AlAs) gap material. For AlAs, there are six ellipsoids along [100] axes with the centers of the ellipsoids located at about three-fourth of the distance from the BZ center. By choosing a proper growth direction (i.e. [110] direction), due to the anisotropic band structures, it is possible to realize large area normal incident excitation of intersubband transitions in the type-II quantum well structures. In this Chapter we describe the first normal incident type-II long wavelength (5 - 18 μm) infrared photodetector using an indirect $AlAs/Al_{0.5}Ga_{0.5}As$ quantum well structure grown by molecular beam epitaxy (MBE) on [110] GaAs substrate.

9.2 Sample Preparation

Unlike the typical direct type-I GaAs/AlGaAs system, we use the larger energy bandgap $AlAs$ material as the quantum well layer and $Al_{0.5}Ga_{0.5}As$ as the barrier layers. Since the compound of $Al_xGa_{1-x}As$ becomes an indirect bandgap material for $x > 0.45$, the typical conduction-band minimum would shift from Γ-band into X-band. Figure 9.1 shows a schematic conduction-band diagram for the type-II indirect $AlAs/Al_{0.5}Ga_{0.5}As$ quantum well structure, in which the electrons are confined inside the $AlAs$ layer. The intersubband transition is from the ground bound state E_0 of AlAs quantum well to the quasi-continuum state above the $AlAs/Al_{0.5}Ga_{0.5}As$ barrier.

The type-II QWIP sample was grown on a GaAs substrate by using the molecular beam epitaxy (MBE) technique, along the [110] growth direction. Figure 9.2 shows the basic geometrical orientations for the GaAs crystal material. A 1.0 μm thick n-GaAs buffer layer of $N_d = 2 \times 10^{18}$ cm^{-3} was first grown on a S.I. [110] GaAs substrate, followed by the growth of a 20-period of $AlAs$ quantum wells with a well width of 30 Å and doping concentration of 2×10^{18} cm^{-3}. The barrier layer on each side of the quantum well consists of an undoped $Al_{0.5}Ga_{0.5}As$ (500 Å) layer. Finally, an n-GaAs cap layer of 0.3 μm thick and dopant density of 2×10^{18} cm^{-3} was grown on top of the MQW/SL layer structure to facilitate ohmic contacts. In the $Al_xGa_{1-x}As$ alloy

system the column-III (Ga,Al) atoms and the column-V (As) atoms are placed in two separate fcc lattices displaced from each other by one-quarter of a body diagonal. The change in lattice constant from $Al_{0.5}Ga_{0.5}As$ to $AlAs$ is very small (about 0.06% at room temperature). There exists a long-range order in the crystal with the sites $0, 0, 0$ and $\frac{1}{2}, \frac{1}{2}, 0$ in each unit cell preferred by Ga atoms and the sites $\frac{1}{2}, 0, \frac{1}{2}$ and $0, \frac{1}{2}, \frac{1}{2}$ preferred by Al atoms. For $Al_{0.5}Ga_{0.5}As$, the structure consists of alternating AlAs and GaAs monolayers when viewed along the [110] growth direction.

9.3 Theory

To understand the basics of the normally induced intersubband transitions and the corresponding indirect type-II quantum well infrared photodetectors, we start with the Hamiltonian description of quantum mechanics for an electron [64]

$$H_o = \frac{p^2}{2m} + V(\mathbf{r}) + \frac{\hbar}{4m^2c^2}\sigma \cdot (\nabla V(\mathbf{r}) \times \mathbf{p}) \tag{9.1}$$

where m, p, and σ are the mass, momentum, and spin operators on an electron, respectively. $V(\mathbf{r})$ is a periodic potential function. The system under consideration consists of an assembly of electrons and the infrared radiation field. The Hamiltonian of this system, $\mathcal{H}$, may be written as the sum of the unperturbed Hamiltonian $\mathcal{H}_0$ and the perturbing Hamiltonian $\mathcal{H}'$ which represents the interaction between the electrons and the incident infrared photon

$$\mathcal{H} = \mathcal{H}_o + \mathcal{H}'_{rad} \tag{9.2}$$

The matrix element of intersubband transition in the quantum well is given by [64,65]

$$M_{fi} = \int \phi_{kf} H'_{rad} \phi_{ki} d\mathbf{r} = -q(\frac{2\pi}{Vcn\hbar\omega})^{1/2} \mathbf{e}_\omega \cdot \nabla_{\mathbf{k}} \mathcal{E}_{\mathbf{k}} \tag{9.3}$$

where the parameters i and f denote the initial and final states, $\mathbf{e}_\omega$ is the unit polarization vector of the incident photon, ω the light frequency, q the electronic charge, V the volume of the crystal, n the refractive index, and $\mathcal{E}$ is the electron energy.

It can be shown that the intersubband transition probability $\eta_{\mathbf{k}}$ may be expressed as [61,66]

$$
\begin{aligned}
\eta_{\mathbf{k}} &= \frac{2\pi}{\hbar}|M_{fi}|^2 \delta(E_f - E_i - \hbar\omega) \\
&= \frac{B_0 k_z^2}{\omega} \left[\frac{\partial^2 \mathcal{E}_{\mathbf{k}}}{\partial k_z \partial k_x} (\mathbf{e}_\omega \cdot \mathbf{x}_0) + \frac{\partial^2 \mathcal{E}_{\mathbf{k}}}{\partial k_z \partial k_y} (\mathbf{e}_\omega \cdot \mathbf{y}_0) + \frac{\partial^2 \mathcal{E}_{\mathbf{k}}}{\partial k_z \partial k_z} (\mathbf{e}_\omega \cdot \mathbf{z}_0) \right]^2 \\
&\quad \times \delta(E_f - E_i - \hbar\omega)
\end{aligned}
\tag{9.4}
$$

where B_0 is a constant equal to $\frac{q^2 \pi^2}{cVn\hbar^2}$; $\mathbf{x}_0$, $\mathbf{y}_0$, and $\mathbf{z}_0$ are the directional unit vectors.

For an indirect type-II AlAs quantum well layers grown along [110] direction, due to the tilted anisotropic energy band with minimum point away from center, the second partial derivatives $\frac{\partial^2 \mathcal{E}_{\mathbf{k}}}{\partial k_z \partial k_i}$ (i = x, y) can be different from zero. Therefore, it is possible to excite long wavelength intersubband transitions in the quantum well under normal incident illumination. However, for a direct type-I system i.e. GaAs due to the isotropic spherical energy surface and the axis symmetrical parabolic band $E = E_z + \hbar^2 (k_y^2 + k_z^2)/2m^*$, it always has $\frac{\partial^2 \mathcal{E}_{\mathbf{k}}}{\partial k_z \partial k_i} = 0$, (where $i \neq z$). The corresponding transition probability becomes

$$
\eta_k = \frac{B_0 k_z^2}{\omega} \left[\frac{\partial^2 \mathcal{E}_{\mathbf{k}}}{\partial k_z \partial k_z} (\mathbf{e}_\omega \cdot \mathbf{z}_0) \right]^2 \delta(E_f - E_i - \hbar\omega)
\tag{9.5}
$$

Equation (9.5) reveals that the optical transition would become zero for type-I structures under normal incident illumination. Therefore, it is advantageous for the type-II GaAs quantum well system to have non-zero cross partial derivatives and normal incident excitation of intersubband transitions along [110] growth direction. Similar properties can also be found in indirect SiGe/Si [16,67] and other material systems [17].

9.4 <u>Experiment and Discussions</u>

Device characterization was performed in a liquid-helium cryogenic dewar. An HP4145 semiconductor parameter analyzer was used to measure the dark current vs. voltage (I-V) curves. Figure 9.3 shows the measured dark I-V curves for temperatures between 68 and 89 K. Substantial reduction in device dark current was achieved in the present type-II structure.

The infrared absorption of our sample was measured at room temperature using a Perkin-Elmer Fourier transform infrared (FTIR) spectrometer. Figure 9.4 (right) shows the result of a room temperature absorption spectrum measurement under normal incidence. The peak absorbance mA = - 1000 log_{10}[transmission] was found to be 20 mAbs , which corresponds to a transmission reduction of $\Delta T/T = 4.5\%$. The peak absorption coefficient is found to be $\alpha = 434.5$ cm^{-1} for the present sample. The absorption peak is at $\lambda = 13.7\mu$m with a spectral range of 9.5 – 18 μm. The results are in a good agreement with our theoretical calculation.

To facilitate the normal infrared illumination, an array of 210 $\times$ 210 μm^2 mesas were chemically etched down to n$^+$-GaAs buffer contact layer on the GaAs substrate. Finally, AuGe/Ni/Au ohmic contact was formed on top of the sample, leaving a central sensing area of 190 $\times$ 190 μm^2 for normal illumination. The photocurrent was measured using a CVI Laser Digikrom 240 monochromator and an ORIEL ceramic element infrared source. Figure 9.4 (left) shows the normalized responsivity versus wavelength measured at T = 25 K. The peak wavelength was found at $\lambda_p = 12.8$ μm with a peak responsivity of $R_p = 24$ mA/W at $V_b = 2.7$ V and T = 25 K, with an IR spectral response range extended from 8 to 18 μm.

Another advantage of using type-II QW structure is that it can provide an important multiple-spectral capability. It arises from the interesting cross-interface transition and Γ-X band interference, as illustrated in Figure 9.5. A low temperature photoluminescence measurement showed a couple of photoemission peaks, including

the visible (Figure 9.6) and near infrared (Figure 9.7) regions. By performing spectral response measurements over the wavelengths from 400 nm to 4 μm, we found two extra shorter wavelength response peaks (B and C as shown in Figure 9.8). One peak is at $\lambda_p = 0.8$ μm, with an open-circuit photovoltaic responsivity $R_\lambda = 0.4$ A/W at T = 25 K. The spectral range covers from visible ($\lambda = 0.5$ μm) to near infrared (NIR) at $\lambda = 1.27$ μm. Another peak was found in the mid infrared (MIR) at $\lambda_p = 2.22$ μm, with a spectral range covering from $\lambda = 1.97$ to 3.2 μm. The peak responsivity was found to be $R_\lambda = 64$ mA/W at $V_b = 5.8$ V and T = 25 K. The multiple spectral responses are attributed to the type-II cross-interface transition [68], different masses ($m_\parallel = 1.1$ m_0 and $m_\perp = 0.19$ m_0), as well as the X- and Γ-band interactions [69] in the indirect quantum well structure. The advantageous normal illumination, together with the extremely broad and multiple-spectral responses, make this indirect type-II QWIP unique and attractive for many infrared applications.

9.5 Conclusion

In conclusion, we have successfully demonstrated the first type-II conduction band QWIP by using an indirect X-band $AlAs/Al_{0.5}Ga_{0.5}As$ system. The front normal incidence is allowed due to the tilted and anisotropic energy band structure grown on the [110] GaAs substrate. A novel multi-spectral photoresponse has been observed, with spectral range covering from $\lambda = 500$ nm to 18 μm. Using the type-II AlAs/AlGaAs QW structures described in this chapter, a new class of normal incidence, large area, high uniformity infrared detectors and imaging arrays can be expected.
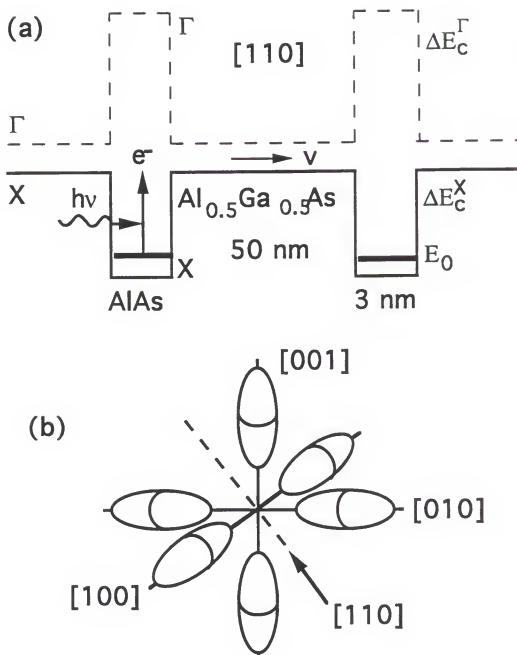
Figure 9.1 (a) Schematic energy band diagram for the type-II QWIP by using AlAs/AlGaAs system. The solid lines represent the X-band edge while the dashed lines indicate the direct Γ-band. (b) The six ellipsoids of X-band conduction band minima of AlAs. The preferred [110] growth direction is indicated by the arrow.
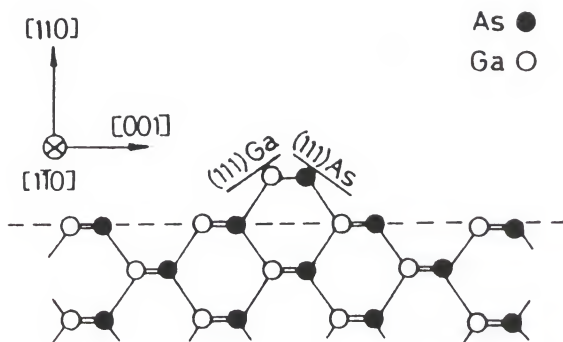
Figure 9.2 The geometrical configuration of the GaAs crystal wafer.
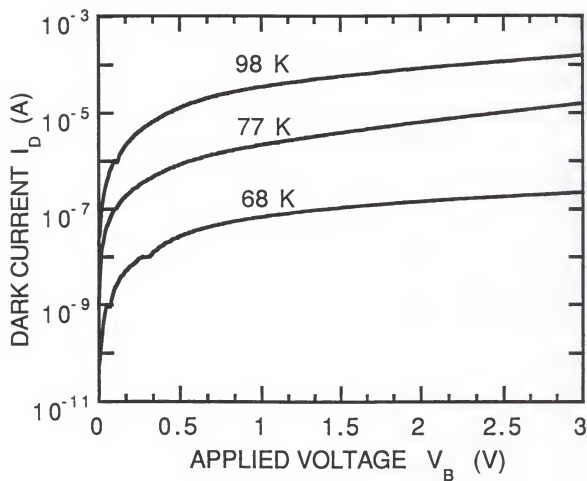
Figure 9.3 The measured dark current versus applied bias voltage for T = 68. 77, 89 K, respectively.
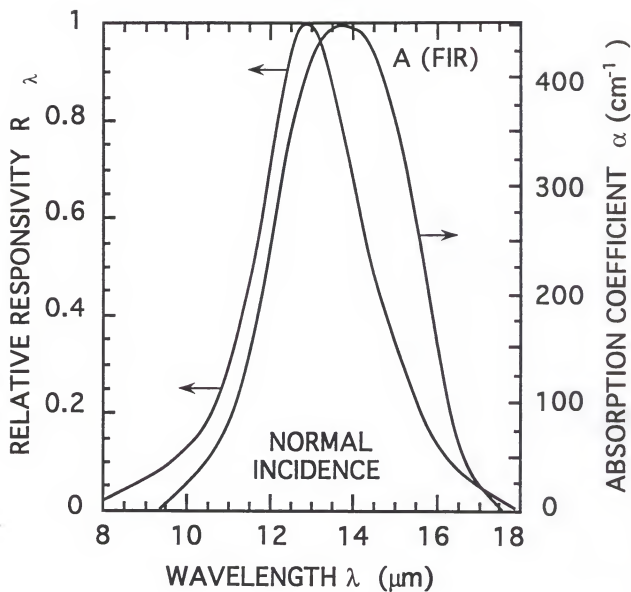
Figure 9.4 The normalized spectral responsivity (left) measured at $V_b = 3$ V and $T = 20$ K. The measured room temperature intersubband absorbance versus wavelength by FTIR spectroscopy (right) at normal incidence.
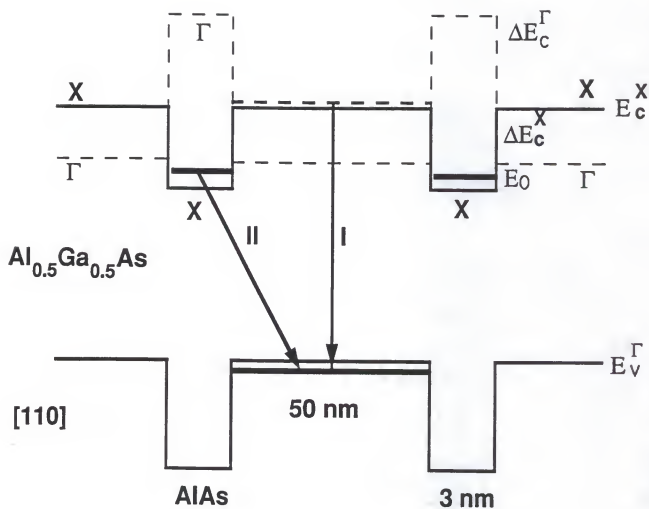
Figure 9.5 The two types of conduction-valence band transitions in the type II quantum well structure.
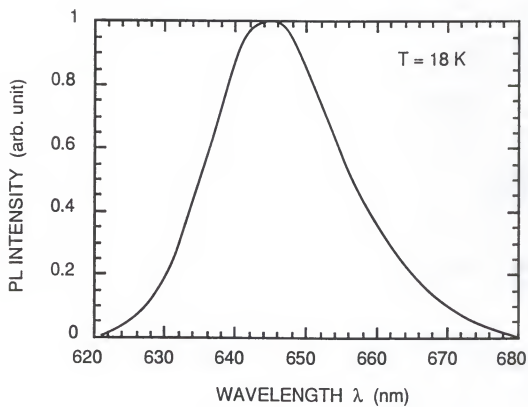
Figure 9.6 Visible photoluminescence spectrum of the sample.
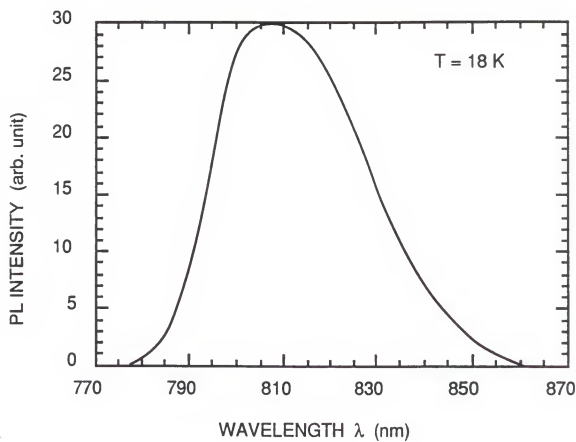
Figure 9.7 Near infrared (NIR) photoluminescence emission.
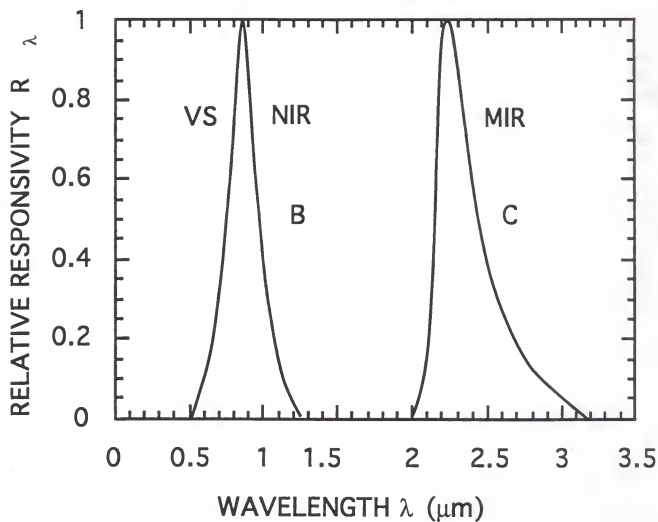
Figure 9.8 Measured multiple spectral responses of the indirect type-II QWIP in visible, near-infrared (NIR) and mid-infrared (MIR) regions.

CHAPTER 10
SUMMARY AND SUGGESTIONS FOR FUTURE WORK

In summary, current status and recent advances in QWIPs based on enlarged quantum wells and miniband transport were reviewed. Three different quantum well infrared photodetector structures, namely BTM, SBTM, and GBTM transition schemes, have been investigated. A detailed study of optimal coupling efficiency versus grating periodicity has also been performed in the front and backside surface illuminated GaAs/AlGaAs QWIPs.

The introduction of superlattice miniband into QWIPs offers a great deal of design flexibility and improved device performance. Two issues that will continue to remain critical in the III-V quantum well infrared detector area in the near future are: 1) dark current; and 2) normal incidence. We have already seen the effect of dark current suppression by tailoring the superlattice space and position in the quantum well structures, and by using the basic bound-to-miniband transition mechanism. New superlattice configurations may also be considered to further optimize the device performance. Beside the metal gratings, dielectric grating couplers and other types of infrared couplers could be useful in coupling radiation into GaAs/AlGaAs multiple quantum well layers. In addition, the shape and the filling factor of a grating coupler play very important roles in the overall coupling efficiency.

Our recent study of indirect material systems show that AlAs/AlGaAs quantum well system has the capability of normal incidence. It may be easier and more straightforward than coupling radiation to GaAs/AlGaAs quantum well layers. Further research in this area may lead to a new and interesting class of large area, normal incidence quantum well infrared detectors and image sensor arrays.

The investigation of heterojunction of internal photoemission approach offers a potential option for long wavelength infrared detection. This approach provides a relative simple device technology that promises producible and uniform focal plane arrays. Further investigation of both III-V and Si-based heterojunctions grown by MBE, in which the barrier can be tailored to the desired cutoff wavelength, is needed.

The valence band structure of GaAs (and related alloys) is also attractive for achieving a normal illumination, though at present the photoresponsivity is relatively small. The light and heavy hole bands become parallel at values of wave vector $\mathbf{k}$ away from the zone center, separated by a constant energy about 80 meV along the [100] direction. The parallel E-$\mathbf{k}$ behavior leads to a large joint density of states, and gives rise to a large absorption coefficient α for photon energy $h\nu$ equal to this separation.

Most of the QWIPs discussed in the literature have been photoconductors, there are, however, various alternatives to be considered, which include: photovoltaic diodes and phototransistors. The interesting feature of photovoltaic detectors are the low operation bias, low dark current, and low power dissipation. On the other hand, the high photocurrent gain β of the phototransistors would be attractive for certain infrared applications.

The negative differential resistance exhibited by the superlattice structures and miniband transport implies that they may be very useful in realizing the next generation of high-speed oscillators, mixers, and logic devices. The operation frequency up to THz has recently been suggested on these devices, which may lead to new electronic applications in the future.

APPENDIX A
THE CHANGES OF ENERGY STATES WITH AN EXTERNAL FIELD
AND INTERNAL ELECTRON-ELECTRON INTERACTION

I. Solution of Schrödinger Equation under An Electric Field

The problem of a charged particle in a uniform static field has been considered in a number of articles. It is found that if in addition the particle is solution can be obtained for any value of the static field. This is a consequence of the very simple and severe boundary conditions imposed upon the wave function $\psi(z)$ for any field. The Schrödinger equation can be written

$$-\frac{\hbar^2}{2m^*}\frac{d^2}{dz^2}\psi(z) - (W + eFz)\psi(z) = 0 \tag{A.1}$$

The zero-field solutions are known, i.e.,

$$W_n = \frac{\hbar^2}{2m^*}[n\frac{\pi}{L_z}]^2, \tag{A.2}$$

$$\psi_n(z) = [\frac{2}{L_z}]^{1/2}cos[n\frac{\pi}{L_z}]^2 \tag{A.3}$$

The ground state is given as

$$W_1 = \frac{\hbar^2}{2m^*}[\frac{\pi}{L_z}]^2 \tag{A.4}$$

and as the unit of field F_1 such that $eF_1L_z = W_1$.

In order to transform the Schrödinger equation into the Airy differential equation is is convenient to use the new variable Z:

$$Z = -[\frac{2m^*}{(e\hbar F)^2}]^{1/3}(W + eFz) \tag{A.5}$$

105

Note that $W + eFz$ represents the kinetic energy and that $[(e\hbar F)^2/2m^*]^{1/3}$ has the dimensions of an energy. Z is therefore a normalized kinetic energy. The new form of Schrödinger equation is written as

$$\frac{d^2}{dZ^2}\psi(Z) - Z\psi(Z) = 0 \tag{A.6}$$

whose solution are of the form

$$\psi(Z) = aAi(Z) + bBi(Z) \tag{A.7}$$

where a and b are two constants and $Ai(Z)$ and $Bi(Z)$ are the Airy functions. The boundary conditions are

$$\psi(Z_+) = \psi(Z_-) = 0 \tag{A.8}$$

where $Z_\pm = Z(\pm L_z/2)$. If we measure the energies and field in units W_1 and F_1, i.e.,

$$w = \frac{W}{W_1}, \qquad f = \frac{F}{F_1} \tag{A.9}$$

then

$$Z_+ = [-\frac{\pi}{f}]^{2/3}(w \pm f/2) \tag{A.10}$$

and

$$0 = Ai(Z_+)Bi(Z_-) - Ai(Z_-)Bi(Z_+) \tag{A.11}$$

which completely determines the eigen energy.

II. Exchange Energy

Here we consider the effect of electron-electron interactions in a doped quantum wells where we expected that charge neutrality will minimize direct Coulomb interactions. In this situation we expect exchange interactions to contribute the most important correction to the usual non-interacting electron approximation. One-electron wave function approximation is assumed. The Hartree-Fock relation with direct and

exchange Coulomb interaction terms and an attractive donor ion-electron interaction is given as

$$\frac{hbar^{-2}}{2m^*}\Delta^2\psi_m(\mathbf{r}) + V(\mathbf{r})\psi_m(\mathbf{r}) + U^{ion}(\mathbf{r})\psi_m(\mathbf{r}) + \sum_n\int d\mathbf{r}'\frac{e^2}{4\pi\epsilon|\mathbf{r}-\mathbf{r}'|}|\psi_n(\mathbf{r}')|^2\psi_m(\mathbf{r})$$

$$-\sum_n\int d\mathbf{r}'\frac{e^2}{4\pi\epsilon|\mathbf{r}-\mathbf{r}'|}\psi_n^*(\mathbf{r}')\psi_m(\mathbf{r}')\psi_n(\mathbf{r})\delta_{s_ms_n} = E_m\psi_m(\mathbf{r}) \tag{A.12}$$

where the Kronecher δ vanishes except for identical spin states, and ϵ is the dielectric constant. U^{ion} is the sum over Coulomb potentials of impurity ions. The fourth and fifth terms of the above equation are the direct and exchange Coulomb interaction terms, respectively. The exchange interaction energy term associated with an electron in the ground state subband, due to all other electrons inside the subband, is given by

$$E_{Xch} = -\frac{e^2}{2\epsilon}\int_0^{k_F}\frac{d^2k'}{(2\pi)^2}\int\frac{exp(-q|x-x'|)}{q}|\phi_0(x')|^2|\phi_0(x)|^2dx' \tag{A.13}$$

where $q = |\mathbf{k}-\mathbf{k}'|$, $k_F = \sqrt{2\pi\rho}$ and ρ is the two-dimensional electron density in the quantum well. By applying the first two terms of the Taylor series expansion, it can be shown that the exchange energy term has the expressions at $k = 0$ and $k = k_F$

$$E_{Xch}(0) = -\frac{e^2k_F}{4\pi\epsilon}[1 - 0.31(k_F/k_1)] \tag{A.14}$$

and

$$E_{Xch}(k_F) = -\frac{e^2k_F}{4\pi\epsilon}[2/\pi - 0.31(k_F/k_1)] \tag{A.15}$$

At a high doping concentration, the exchange energy term dominates the direct Coulomb interaction term. Since the exchange interaction is attractive, the ground state energy levels are shifted downward. The photon energies at which intersubband transition is determined by

$$h\nu = E_2 - E_1 - E_{Xch} \tag{A.16}$$

where E_2 and E_1 represent the two subband energy states for intersubband infrared transition.

APPENDIX B
TWO-DIMENSIONAL DENSITY OF STATES

The z-direction energy eigenfunction of carriers in a two-dimensional (2-D) superlattice can be expressed as $\psi(z) = e^{ik_z z}u_k(z)$ within the envelope-function approximation, where k_z is the wave number in the z direction and $u_k(z)$ is a periodic function satisfying $u_k = u_k(z + d)$. Here $d = a_z + b_z$ are the well and barrier widths, respectively. By applying the periodic boundary condition $\psi(Md) = \psi(0)$ and the relation $u_k(MD) = u_k(0)$, we obtain $k_z = 2m\pi/Md$ with $m = 0, \pm1, \pm2, \cdots$. Thus the interval Δk_z between adjacent states is given by $\Delta k_z = 2\pi/Md$. The density of states (DOS) can be expressed as

$$
\begin{aligned}
g_2(E) &= 2\left(\frac{1}{\Delta k}\right)\frac{d}{dE}\left[\frac{1}{L_x L_y L_z}N(E)\right] \\
&= \frac{2}{\pi^3}\frac{d}{dE}\left[\int_{E_{z,1}^{min}}^{E}(\frac{\partial k_z}{\partial E_z})dE_z \int_0^{E-E_z}(\frac{\partial k_y}{\partial E_y})dE_y \int_0^{E-E_y-E_z}(\frac{\partial k_x}{\partial E_x})dE_x\right]
\end{aligned} \quad \text{(B.1)}
$$

Here L_x, L_y and $L_z = Md$ are the sizes of the superlattice structure in the x, y, and z directions, $\Delta k = (2\pi/L_x)(2\pi/L_y)(2\pi/L_z)$ represents the unit volume occupied by a state in the k space, $N(E)$ represents the volume in k space that the states with $E < E_b$ occupies, and the factor 2 represents the spin degeneracy. $dN(E)/dE$ represents the density of volume in k space per unit energy at an energy E. By using the relations $E_x = (\hbar k_x)^2/2m^*$, $E_y = (\hbar k_y)^2/2m^*$, $k_z(E_{z,1}^{min}) = 0$, and the formula

$$
\int(\frac{a-x}{x})^2 dx = (ax - x^2)^{1/2} - a\sin^{-1}(\frac{a-x}{x})^2 \quad \text{(B.2)}
$$

it can be shown that final expression of two-dimensional density of states (DOS) is given as

$$
g_2(E) = (m^*/\pi^2\hbar^2)k_z(E) \quad \text{(B.3)}
$$

108

Although the above equation was obtained for 2-D superlattices, it can also be applied to bulk media. For bulk media, $k_z(E) = (2m^*E)^{1/2}/\hbar$ yields

$$g_2(E) = \frac{1}{2\pi^2}\left(\frac{2m^*}{\hbar^2}\right)^{3/2} E^{1/2} \tag{B.4}$$

which is just the three-dimensional (3-D) density of states. For multiple quantum wells and superlattices, $k_z(E)$ should be obtained from the $E_z - k_z$ relation and by replacing the E_z with E. At $E = E_z^{max}$, specifically, we readily have 2-D density of states

$$g_2 = \frac{m^*}{\pi\hbar^2 d} \tag{B.5}$$

since $k_z(E) = \pi/d$, which is the wave number at the Brillouin zone edge.

APPENDIX C

MATRIX METHOD FOR OPTICAL WAVEGUIDE QW DETECTORS

Recently there has been an intensive interest in waveguide enhanced long wavelength quantum well infrared detectors. A significant improvement of quantum efficiency has been reported due to the better confinement of infrared radiation within the waveguide structure.

It is well known that optical wave is essentially confined in the transverse direction and guided along the longitudinal direction. The change in the index profile is assumed to be small and proportional to the composition profile in the case of AlAs/AlGaAs/GaAs waveguides. The index profiles can be obtained numerically by using multi-layer matrix method.

We discuss below the waveguide system without gain or loss. We can describe the index profile of a z direction invariant waveguide in the form

$$\epsilon(x, y) = \epsilon_0 \cdot n^2(x, y) \tag{C.1}$$

The electromagnetic field of those guided mode propagating in the waveguide are

$$\vec{E}(x, y, z) = \vec{E}(x, y, z) \cdot e^{-j\beta z} \tag{C.2}$$

$$\vec{H}(x, y, z) = \vec{H}(x, y, z) \cdot e^{-j\beta z} \tag{C.3}$$

In planar waveguide, the fields are confined to one dimension only, say x direction, thus

$$\frac{\partial \vec{E}}{\partial y}(x, y) = \frac{\partial \vec{H}}{\partial y}(x, y) = 0 \tag{C.4}$$

A planar waveguide support two kinds of guided modes. One of them is TE(transverse electric) mode which has no longitudinal electric field($E_z = 0$), the other is TM(transverse

110

magnetic) mode which has no longitudinal magnetic field($H_z = 0$). Once we obtain the field of TM mode, we can get the field solution of TE mode by duality

$$\vec{E} \longrightarrow \vec{H} \qquad \vec{H} \longrightarrow -\vec{E} \tag{C.5}$$

$$\epsilon \longrightarrow \mu \qquad \mu \longrightarrow \epsilon \tag{C.6}$$

Therefore, we discuss TM mode only.

First, we put Maxwell equation into transversal component and longitudinal component

$$\nabla_t \times \vec{E}(x,y) + j\omega\mu \cdot \vec{H}(x,y) = j\beta\hat{z} \times \vec{E}_t(x,y) \tag{C.7}$$

$$\nabla_t \times \vec{H}(x,y) - j\omega\epsilon \cdot \vec{E}(x,y) = j\beta\hat{z} \times \vec{H}_t(x,y) \tag{C.8}$$

For TM mode, there exists three field H_y, E_x and E_z. The above two equations reduce to

$$x \quad : \qquad \beta \cdot H_y = \omega\epsilon E_x \tag{C.9}$$

$$z \quad : \qquad \frac{\partial H_y}{\partial y} = j\omega\epsilon E_z \tag{C.10}$$

$$y \quad : \qquad \frac{\partial E_z}{\partial x} + j\beta E_x = j\omega\epsilon H_y \tag{C.11}$$

Set U $= H_y$ and V$= \omega E_z$ we have

$$\frac{dU}{dx} = j \cdot \epsilon V \tag{C.12}$$

$$\frac{dV}{dx} = j(\beta^2 - n^2 \cdot k_0^2)U \tag{C.13}$$

Both U and V obey the transverse wave equation

$$U'' = (\beta^2 - n^2 \cdot k_0^2)U \tag{C.14}$$

Thus, the general solution are

$$U = A \cdot e^{-j\gamma x} + B \cdot e^{j\gamma x} \tag{C.15}$$

$$V = \frac{\gamma}{\epsilon}A \cdot e^{-j\gamma x} - \frac{\gamma}{\epsilon}B \cdot e^{j\gamma x} \tag{C.16}$$

where

$$\gamma^2 = n^2 \cdot k_0^2 - \beta^2 \tag{C.17}$$

For one film, three-layer planar waveguide, we can try to solve the wave equation by set

$$U_0 = U(0) \tag{C.18}$$

$$V_0 = V(0) \tag{C.19}$$

at x =0, and get

$$\begin{pmatrix} U_0 \\ V_0 \end{pmatrix} = M \begin{pmatrix} U \\ V \end{pmatrix} \tag{C.20}$$

where

$$M = \begin{pmatrix} \cos \gamma x & \frac{j \cdot \epsilon}{\gamma} \sin \gamma x \\ \frac{j \gamma}{\epsilon} \sin \gamma x & \cos \gamma x \end{pmatrix} \tag{C.21}$$

is the characteristic matrix. For m-layer waveguide, each has its width d_i

$$M_i = \begin{pmatrix} \cos \gamma_i x & \frac{-j \epsilon_i}{\gamma_i} \sin \gamma_i x \\ \frac{-j \gamma_i}{\epsilon_i} \sin \gamma_i x & \cos \gamma_i x \end{pmatrix} \tag{C.22}$$

where i =1,....,m-2. Thus

$$\begin{pmatrix} U_0 \\ V_0 \end{pmatrix} = M_1|_{d_1} \cdots M_{m-2}|_{d_{m-2}} \begin{pmatrix} U \\ V \end{pmatrix} \tag{C.23}$$

To be a guided mode, the electromagnetic fields in the substrate are evanescent wave and have the form

$$\begin{aligned} U_s &= A \cdot e^{\alpha_s x} \\ V_s &= j\alpha_s A \cdot e^{\alpha_s x} \end{aligned} \tag{C.24}$$

So does the electromagnetic field in the cover

$$\begin{aligned} U_c &= A \cdot e^{-\alpha_c x} \\ V_s &= -j\alpha_c A \cdot e^{\alpha_c x} \end{aligned} \tag{C.25}$$

Finally we write down the matrix expression

$$\begin{pmatrix} A \\ j\alpha_s A \end{pmatrix} = \begin{pmatrix} m_{11} & m_{12} \\ m_{21} & m_{22} \end{pmatrix} \cdot \begin{pmatrix} B \\ -j\alpha_c B \end{pmatrix} \tag{C.26}$$

and the dispersion relation for a multilayer slab waveguide is

$$j(\alpha_s m_{11} + \alpha_c m_{22}) = m_{21} - \alpha_s \alpha_c m_{12} \tag{C.27}$$

In ray optics, the angle of optical ray propagate in a waveguide is expressed as

$$\cos\theta = \frac{\beta}{k_0} \tag{C.28}$$

We can adjust the width of each layer to obtain the propagation angle we need.

APPENDIX D
ABSORPTION IN A PARABOLIC QUANTUM WELL

Consider the Schrödinger equation for a parabolic quantum well with a uniform applied electric field

$$\left(-\frac{hbar^2}{2m^*}\frac{\partial^2}{\partial z^2} + \frac{K}{2}z^2 - eFz\right)\psi(z,t) = i\hbar\frac{\partial}{\partial t}\psi(z,t) \tag{D.1}$$

where $e = -|e|$, m_c^* is the effective mass of the electrons in the conduction band, and K is the curvature parameter for the conduction band. If the applied electric field is a dc field, the solutions of the Schrödinger equation are those of a displaced harmonic oscillator:

$$\psi_n(z,t) = (\alpha/\sqrt{\pi}2^n n!)^{1/2} exp[-\alpha^2(z-z_0)^2/2] \times H_n[\alpha(z-z_0)]exp[-iE_n t/\hbar] \tag{D.2}$$

where

$$\alpha = \left(\frac{m^*\omega_0}{\hbar}\right)^{1/2}, \quad \omega_0 = \left(\frac{K}{m^*}\right), \quad z_0 = \frac{eF}{K} \tag{D.3}$$

and the energy is given as

$$E_n = (n+\frac{1}{2})\hbar\omega_0 - (K/2)z_0^2 \tag{D.4}$$

where $n = 0, 1, 2, \cdots$.

In general, the linear optical absorption coefficient α and the change in the refractive index can be obtained from the Fermi golden rule or the density matrix approach:

$$\alpha = (\omega/cn_r\epsilon_0)Im[\epsilon_0\chi_{ij}(\omega)] \tag{D.5}$$

$$\Delta n = (1/2n_r\epsilon_0)Re[\epsilon_0\chi_{ij}(\omega)] \tag{D.6}$$

where

$$\epsilon_0\chi_{ij}(\omega) = \frac{2}{V}\sum_{m,n}\sum_{k_t^{(m)}}\sum_{k_t^{(n)}}\frac{(er_i)_{mn}(er_j)_{nm}}{[E_n(k_t^{(n)}) - E_m(k_t^{(n)}) - \hbar\omega] - i(\Gamma_{mn}/2)}(f_m - f_n) \quad (D.7)$$

$$E_n(k_t^{(n)}) = E_n + (\hbar k_t^{(n)})^2/2m^* \quad (D.8)$$

For intersubband optical transitions, Eq. 7 reduces to:

$$\epsilon_0\chi_{33}(\omega) = \sum_m\sum_n\frac{|ez_{mn}|^2}{(E_n - E_m - \hbar\omega) - i(\Gamma_{mn}/2)} \times (N_m - N_n) \quad (D.9)$$

where N_m is the electron density of the mth subband:

$$N_m = \frac{2}{V}\sum_{k_t}\frac{1}{1 + exp[E_F - E_m(k_t)]/k_Bt} \quad = \frac{m^*k_BT}{\pi\hbar^2L}ln[1 + exp(\frac{E_F - E_m}{k_BT})] \quad (D.10)$$

where k_B is the Boltzmann constant and L is the effective width in the z direction.

The net intersubband absorption coefficient α in the parabolic quantum well is given by

$$\alpha(\omega) = \frac{\omega N}{cn_r\epsilon_0}(\frac{e^2\hbar}{2m^*\omega_0})\frac{\Gamma/2}{(\hbar\omega_0 - \hbar\omega)^2) + (\Gamma/2)^2} \quad (D.11)$$

where

$$N = \sum_{m=0}^{\infty}N_m \quad (D.12)$$

is the total carrier concentration in the quantum well.

PROGRAM FOR THE QUANTUM WELL MODELING AND
CHARACTERIZATION

```
****************************************************************
* THIS PROGRAM IS DESIGNED FOR QUANTUM WELL AND SUPERLATTICE
* CALCULATIONS AND QUANTUM WELL INFRARED DETECTOR CHARACTER-.
* IZATION. IT CAN GIVE THE TRANSMISSION COEFFICIENT, EIGENSTATE
* ENERGIES, AND RELATIVE DESITY OF STATES IN GaAs/AlGaAs AND
* OTHER III-V MULTIQUANTUM WELL AND SUPERLATTICE STRUCTURES.
****************************************************************
C
        COMPLEX S11(502),S12(502),S21(502),S22(502)
        COMPLEX P11(502),P12(502),P21(502),P22(502)
        REAL TH(502),RATIO(502),XV(50),D(300),V(300)
        REAL EIGEN(20),VEGN(20)
        COMPLEX R1,T1,CC,A11,A12,A21,A22
        COMPLEX FJ,FKX1,FKX2,DLT1
        DOUBLE PRECISION  FK,EFF,D1,D2,EM,DFN
        CHARACTER TEXT
        FJ=(0.,1.)
3       FORMAT(A1)
        DO 5 I=1,300
        V(I)=0.
5       D(I)=0.
        NUM=502
        EFF=DBLE(0.0665)
        FK=1.620078411*SQRT(EFF)*1.D-2
        L1=0
*** Potential Profile ***
        NTL=0
        NSL1=2
        D(1)=0.0
        V(1)=0.0
11      CONTINUE
14      CONTINUE
**********************************
*       QW CELL PROFILE
```

```
***********************************
      PRINT*, 'QW CELL PROFILE'
      I7A=2
      OPEN(03,FILE='PTLN.DAT')
      OPEN(02,FILE='PTL.DAT')




      DO 58 I=2,49
      READ(02,9944) XV(I),D(I)
9944  FORMAT(F4.2,F5.0)
      WRITE(03,9955) XV(I),D(I)
      IF(XV(I).EQ.999.) GOTO 59
      IC=I
58    CONTINUE
59    DO  959 I=2,IC
      X=XV(I)
      CALL BARR(EC,X)
      V(I)=EC
959    CONTINUE
      CLOSE(02)
      CLOSE(03)
****************************************
****************************************
         LAYER=IC
****
      PRINT *,'Coupling Gap  d2= ?'
      READ(5,*) D(2)
      PRINT *,'STARTING POINT  E1= ?'
      READ(5,*) E1
      PRINT *,'END POINT  E2= ?'
      READ(5,*) E2
      PRINT *,'CAL STEP   = ?'
      READ(5,*) ESTEP
16    LN=1
      NCNT=0
      DO 25 I=1,NUM
      P11(I)=(1.,0.)
      P12(I)=(0.,0.)
      P21(I)=(0.,0.)
      P22(I)=(1.,0.)
      RATIO(I)=0. 0
```

```
        TH(I)=0.0
25      CONTINUE
****************************
***   BEGIN CAL DELTA & KX
****************************
20      I1=0
30      DO 60 FE=E1,E2,ESTEP
        FEM=DBLE(FE)
        DFN=DBLE(V(1))
        D1=DBLE(FEM-DFN)
        IF(D1.LT.0.) THEN
            D1=-D1
            CC=FJ
          ELSE
            CC=(1.,0.)
          ENDIF
        FKX1=SQRT(D1)*CC
        DFN=DBLE(V(2))
        D2=DBLE(FEM-DFN)
        IF(D2.LT.0.) THEN
            D2=-D2
            CC=FJ
          ELSE
            CC=(1.,0.)
          ENDIF
        FKX2=SQRT(D2)*CC
C
*************************************
*  REFLECTION & TRANSMISSION
*************************************
            R1=(FKX1-FKX2)/(FKX1+FKX2)
            T1=2.*FKX1/(FKX1+FKX2)
C
*************************************
*** MATRIX ELEMENTS ***
*************************************
        I1=I1+1
        DLT1=-FJ*FK*D(1)*FKX1
        S11(I1)=CEXP(DLT1)/T1
        S12(I1)=R1*S11(I1)
        S22(I1)=CEXP(-DLT1)/T1
        S21(I1)=R1*S22(I1)
        TH(I1)=FE
        NI=I1
```

```
60      CONTINUE
        DO 70 I=1,NI
        A11=P11(I)*S11(I)+P12(I)*S21(I)
        A12=P11(I)*S12(I)+P12(I)*S22(I)
        A21=P21(I)*S11(I)+P22(I)*S21(I)
        A22=P21(I)*S12(I)+P22(I)*S22(I)
        P11(I)=A11
        P12(I)=A12
        P21(I)=A21
        P22(I)=A22
70      CONTINUE
****************************************
***   NEXT LAYER ***
        IF(LN.GE.LAYER) GOTO 75
        LN=LN+1
        V(1)=V(LN)
        V(2)=V(LN+1)
        D(1)=D(LN)
        GOTO 20
****************************************
*****************
*** BACKWARDS   ***
*****************
75      NCNT=NCNT+1
        IF(NCNT.EQ.2) GO TO 100
        PRINT *,'WHICH LAYER INTERESTED ?  i= ?'
        READ(5,*) ILAY
        DO 80 I=1,NI
        RATIO(I)=ABS(P11(I))
80      CONTINUE
**********************
***  FROM ith LAYER ***
**********************
        LN=ILAY
        V(1)=V(LN)
        V(2)=V(LN+1)
        D(1)=D(LN)
        DO 90 I=1,NUM
        P11(I)=(1.,0.)
        P12(I)=(0.,0.)
        P21(I)=(0.,0.)
        P22(I)=(1.,0.)
90      CONTINUE
        GOTO 20
```

```
*******************************
***   CALCULATE THE RATIO   ***
*******************************
100     CONTINUE
        DO 120 I=1,NI
        TT=ABS(P11(I)/RATIO(I))
        U=TT*TT
        RATIO(I)=U
120     CONTINUE
*******************************
***   LOOK FOR EIGEN LEVELS  ***
*******************************
        NE=0
        FA=RATIO(1)
        FB=RATIO(2)
        DO 130 I=3,NI
        FC=RATIO(I)
        IF(FB.GT.FA.AND.FB.GT.FC) THEN
                NE=NE+1
                EIGEN(NE)=TH(I-1)
                VEGN(NE)=FB
            ELSE
                CONTINUE
            ENDIF
        FA=FB
        FB=FC
130     CONTINUE
*
***********************
***   OUTPUT       ***
***********************
*
*       PRINT 132,'x=',X,'BARRIER VB=',VBB,'meV','Well W=',WWID
*32     FORMAT(1X,A3,F5.3,5X,A12,F8.4,A3,5X,A8,F6.1)
        DO 135 I=NE,1,-1
        PRINT *,I,'E',EIGEN(I),'POWER',VEGN(I)
135     CONTINUE
*
***********************************
***     WAVELENGTH  1GND--EXT.  ***
***********************************
*
*       IF(NE.GE.2) THEN
*       FLMBT=1238.9/(EIGEN(2)-EIGEN(1))
```

```
*         PRINT *, 'E2-E1  WAVELENGTH=',FLMBT
*       ELSE
*         FLMBT=1238.9/(VBB-EIGEN(1)+24.0)
*        PRINT *, 'E0-3D  WAVELENGTH=',FLMBT
*       ENDIF
***        ********** Change below ***
***
        PRINT *,'CHANGES  ? RETN, IF YES'
        READ 3,TEXT
        IF(TEXT.EQ.' '.OR.TEXT.EQ.'Y') GO TO 145
        GO TO 999
145     CONTINUE
***************************************
        OPEN(03,FILE='PTLN.DAT')
        DO 858 I=2,IC
        READ(03,9955) XV(I),D(I)
        PRINT*, XV(I), D(I),'---- 1'
858      CONTINUE
        CLOSE(03)
859      DO  759 I=2,IC
        X=XV(I)
        CALL BARR(EC,X)
        V(I)=EC
759      CONTINUE
        PRINT *,'ANY CHANGE IN WELL-WIDTH ? NO, RTN   --- (again)'
        DO 147 IW=2,IC
            PRINT *,'V(',IW,')=',V(IW), 'NO RTN,  OR PRESS Y'
              READ 3, TEXT
              IF(TEXT.NE.'Y ') GO TO  146
                READ(5,*) X
                XV(IW)=X
                 CALL BARR(EC,X)
                   V(IW)=EC
146          PRINT *,'D(',IW,')=',D(IW), 'NO RTN,  OR PRESS Y'
              READ 3, TEXT
              IF(TEXT.EQ.'Y ') READ(5,*) D(IW)
147          CONTINUE
802      OPEN(03,FILE='PTLN.DAT')
        DO 9958 I=2,IC
        WRITE(03,9955) XV(I),D(I)
9955     FORMAT(1X,F4.2,2X,F5.0)
        PRINT*, XV(I), D(I),'---- 2'
9958     CONTINUE
        CLOSE(03)
```

```
C
****************************************************
*   IN THE FOLLOWING YOU ARE OFFERED OPTIONS
*   TO MAKE A DESIGN CHANGE
****************************************************
C
        PRINT *,'Any Change in Coupling-Gap? NO/RTN -- (again)'
        READ 3,TEXT
        IF(TEXT.NE.' '.OR.TEXT.EQ.'Y') THEN
                PRINT *,'Gap= ?'
                READ(5,*) D(2)
            ELSE
                GO TO 803
            ENDIF
803     PRINT *,'Any Change in Starting Point E1 ?  NO, RTN'
        READ 3,TEXT
        IF(TEXT.NE.' '.OR.TEXT.EQ.'Y') THEN
                PRINT *,'E1= ?'
                READ(5,*) E1
            ELSE
                GO TO 804
            ENDIF
804     PRINT *,'Any Change in Ending Point E2 ?  NO, RTN '
        READ 3,TEXT
        IF(TEXT.NE.' '.OR.TEXT.EQ.'Y') THEN
                PRINT *,'E2= ?'
                READ(5,*) E2
            ELSE
                GO TO 805
            ENDIF
805     CONTINUE
                PRINT *,'STEP= ?'
                READ(5,*) ESTEP
        GO TO 16
*******************************
999     CONTINUE
*
*******************************
*   PUT FINAL DATA ON HARD DISK FOR E+/E0 VS E(X) CURVE
*******************************
*
** OUTPUT RATIO=E+3/E+1:
        OPEN(01,FILE='TND.DAT')
        DO 140 I=1,NI
```

```
       WRITE(01,*) TH(I),RATIO(I)
140    CONTINUE
       STOP
       END
***********************************
***********************************

       SUBROUTINE BARR(EC,X)
       REAL EC,X
       EC=0.65*(1.425*X-0.9*X*X+1.1*X*X*X)*1000.
*       PRINT 3,'X=',X,'EC=',EC,'meV'
*3     FORMAT(1X,A3,F5.3,10X,A4,F9.4,A4)
       RETURN
       END

***********************************
***********************************
```

REFERENCES

[1] L. Esaki and R. Tsu, "Superlattice and negative differential conductivity in semiconductors," IBM J. Res. Develop., **14**, 65 (1970).

[2] R.F. Kazarinov and R.A. Suris, "Possibility of amplification of electromagnetic waves in the semiconductor with a superlattice," Fiz. Tekh. Poluprov., **5**, 797 (1971).

[3] R. Tsu and L. Esaki, Appl. Phy. Lett. **22**, 562 (1973).

[4] L. Esaki and L.L. Chang, Appl. Phy. Lett. **24**, 593 (1974).

[5] F. Capasso, K. Mohammed, A.Y. Cho, R. Hull, A.L. Hutchinson, Appl. Phys. Lett. **47**, 420 (1985).

[6] A. Kastalsky, T. Duffield, S.J. Allen, and J. Harbison, Appl.Phys. Lett. **52**, 1320 (1988).

[7] Byungsung O, J.W. Choe, M.H. Francombe, K.M.S.V. Bandara, and D. D. Coon, Appl. Phys. Lett. **57**, 503 (1990).

[8] H. Sakaki, M. Tsuchiya, and J. Yoshino, Appl. Phys. Lett., **47**, 295 (1985).

[9] L.C. West and S.J. Eglash, Appl. Phys. Lett. **46**, 1156 (1985).

[10] J. S. Smith, L. C. Chiu, S. Margalit, A. Yariv, and A. Y. Cho, J. Vac. Sci.Technol. B **1**, 376 (1983).

[11] B. F. Levine, K.K. Choi, C.G. Bethea, J. Walker, and R. J. Malik, Appl. Phys. Lett. **50**, 1092 (1987).

[12] D.D. Coon and R.P.G. Karunasiri, Appl. Phys. Lett. **33**, 495 (1984).

[13] B.F. Levine, G. Hasnain, C.G. Bethea, and Naresh Chand, Appl. Phys.Lett., **54**, 2704 (1989).

[14] B. F. Levine, C.G. Bethea, G. Hasnain, V.O. Shen, E. Pelve, R.R. Abbott, and S.J. Hsieh, Appl. Phys. Lett. **56**, 851 (1990).

[15] L.S. Yu and S.S. Li, Appl. Phys. Lett. **59**, 1332 (1991).

[16] C.L. Yang, D.S. Pan, and R. Somoano, J. Appl. Phys. **65**, 3253 (1989).

[17] D. Brown and S.J. Eglash, Phys. Rev. B **41**, 7559 (1990).

[18] D. Ahn and S.L. Chuang, Phys. Rev. **B 35**, 4149 (1987).

[19] H.C. Casey, Jr., and M.B. Panish, *Heterostructure Lasers* (Academic Press, New York, 1978).

[20] S.L. Chuang and K. Hess, J. Appl. Phys., **59**, 2885 (1986).

[21] R. Tsu and L. Esaki, Appl. Phy. Lett. **22**, 562 (1973).

[22] R.K. Willardson and A. Beer, *Semiconductors and Semimetals* (Academic Press, San Diego, CA, 1987) V. 24.

[23] G. Bastard, Acta Electron., **25**, 147 (1983).

[24] G. Bastard, Phys. Rev. B **24**, 5693 (1981).

[25] R.F. Lazarinov and R.A. Suris, Sov. Phys. Semicond., **6**, 120 (1972).

[26] A. Seilmerier, H.J. Hübner, M. Wörner, G. Abstreiter, G. Weimann, and W. Schlapp, Solid State Electron. **31**, 767 (1988).

[27] F. Capasso, K. Mohammed, and A.Y. Cho, IEEE J. Quantum Electron. **22**, 1853 (1986).

[28] N.W. Ashcroft and N.D. Mermin, *Solid State Physics* (Holt, Rinehart and Winston, New York, 1976).

[29] D. Delagebeaudeuf, P. Deleckyse, P. Etienne, J. Massiers, M. Laviron, J. Chaplart, and T. Linh, Electron. Lett. **18**, 85 (1982).

[30] I. Hase, H. Kawai, K. Kaneko, and K. Watanabe, Electron. Lett., **20**, 491 (1984).

[31] P. J. Price, IBM J. Res. Develop. **17**, 39 (1973).

[32] M. Artaki and K. Hess, Superlattices and Microstructures **1**, 489 (1985).

[33] A. Harwit, J.S. Harrier, Jr., and A. Kapitulnik, Appl. Phys. Lett., 3211 (1986).

[34] A.K. Ghatak, K. Thyagarajan, M.R. Shenoy, IEEE J. Quantum Electron. **24**, 1524 (1988).

[35] T.K. Gaylord, E. N. Glytsis, and K.F. Brennan, J. Appl. Phys., **65**, 2535 (1989).

[36] G. Hasnain, B.F. Levine, S. Gunapala, and Naresh Chand, Appl. Phys. Lett. **57**, 605 (1990).

[37] K.M.S.V. Bandara, D.D. Coon, and Byungsung O, Appl. Phys. Lett. **53**, 1931 (1988).

[38] W.L. Bloss, J. Appl. Phys. **66** (8), 3639 (1989).

[39] A. Harwit and J.S. Harris, Jr., Appl. Phys. Lett. **50**, 685 (1987).

[40] M.A. Kinch and A. Yariv, Appl. Phys. Lett. **55**, 2093 (1989).

[41] R.B. Darling, ÎEEE J. Quantum Electron. **Q-22**, 1628 (1988).

[42] A.S. Vebgurlekar, F. Capasso, A.L. Hutchinson, and W.T Tsang, Appl. Phys. Lett. **56**, 262 (1990).

[43] L.S. Yu, S.S. Li, and Y.C. Kao, *Proc. 1990 GOMAC* (Las Vegas, NV), 479 (1990).

[44] S.D. Gunapala, B.F. Levine and Naresh Chand, J. Appl. Phys. **70**, 305 (1991).

[45] B.F. Levine, A.Y. Cho, J. Walker, R.J. Malik, D.A. Kleinman, and D.L. Sivco, Appl. Phys. Lett., **52**, 1481 (1988).

[46] H. Asai and Y. Kawamura, Appl. Phys.Lett., **56**, 746 (1990).

[47] G. Hasnain, B.F. Levine, D.L. Sivco, A.Y. Cho, Appl. Phys. Lett., **56**, 770 (1990).

[48] Larry S. Yu, Sheng S. Li, and Pin Ho, Appl. Phys. Lett. **59**, 2712 (1991).

[49] S.M. Sze, *High-Speed Semiconductor Devices* (John Wiley & Sons, New York, 1990).

[50] K. K. Choi, B. F. Levine, R. J. Malik, J. Walker, and C.G. Bethea, Phys. Rev. **B 35**, 4172 (1987).

[51] A. Zussman, B.F. Levine, J.M. Kuo, and J. de Jong, Appl. Phys. Lett., **70**, 5101 (1991).

[52] B.K. Janousek, M.J. Daugherty, W.L. Bloss, M.L. Rosenbluth, M.J. O'Loughlin, H. Kanter, F.J. De Luccia, and L.E. Perry, J. Appl. Phys. **67**, 7608 (1991).

[53] F.H. Julien, P. Vagos, J.-M. Lourtioz, and D.D.Yang, Appl. Phys. Lett., **59**, 2645 (1991).

[54] K.W. Goossen and S.A. Lyon, Appl. Phys. Lett., **53**, 1027 (1988).

[55] G. Hasnain, B.F. Levine, C.G. Bethea, R.A. Logan, J. Walker, and R.J. Malik, Appl. Phys. Lett., **54**, 2515 (1989).

[56] Andersson, L. Lundqvist, and Z.F. Paska, Appl. Phys. Lett., **59**, 859 (1991).

[57] L.S. Yu, S.S. Li, and Y.C. Kao, *Proc. International Electron Devices and Materials Symposium* (Hsinchu, Taiwan), p. 472. (1990).

[58] T.W. Nee and F. Koch, Phys. Rev. **B 29**, 3225 (1984).

[59] D. Maystre and R. Petit, Opt. Commu. **5**, 91 (1972).

[60] R. Petit, *Electromagnetic Theory of Gratings* (Springer-Verlag, Berlin, 1980).

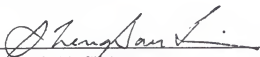[61] D. Ahn and S.L. Chuang, IEEE J. Quantum Electron., **QE-23**, 2196 (1987).

[62] S.J. Allen, Jr., D.C. Tsui, and B. Vinter, Solid State Commun. **20**, 425 (1997).

[63] L.S. Yu, S.S. Li, and Y.C. Kao, J. Appl. Phys. (in press) (1992).

[64] E.O. Kane, J. Phys. Chem. Solid **1**, 249 (1957).

[65] E. Haga and H. Kimura, J. Phys. Soc. Jpn. **18**, 777 (1963).

[66] F. Stern and W.E. Howard, Phys. Rev., **163**, 816 (1967).

[67] K.L. Wang, R.P.G. Karunasiri, S.K. Chun, J.S. Park, and C.H. Lee, *Proc. of Innovative Long-Wavelength Infrared Detector Workshop* (Jet Propulsion Laboratory, Pasadena, CA), p. 43 (April 8, 1992).

[68] P. Dawson, B.A. Wilson, C.W. Tu, and R.C. Miller, Appl. Phys. Lett., **48**, 541 (1986).

[69] M.H. Meynadier, R.E. Nahory, J.M. Worlock, M.C. Tamargo, and J.L. de Miguel, Phys. Rev. Lett., **60**, 1338 (1988).

BIOGRAPHICAL SKETCH

Larry S. Yu was born in Hefei, China, on October 31, 1961. He received the B.S. degree in optical engineering from Zhejiang University, Hangchou, and M.S. degree in optoelectronics from Xian Institute of Optics and Fine Mechanics, China Academics of Sciences, China, in 1982 and 1986, respectively.

In January 1987, he enrolled in the University of Florida Graduate School as a Ph.D. student. After two years of graduate study, he joined the semiconductor device research group in the Department of Electrical Engineering. Since then he has been working toward the Ph.D. degree in electrical engineering at the University of Florida.

I certify that I have read this study and that in my opinion it conforms to acceptable standards of scholarly presentation and is fully adequate, in scope and quality, as a dissertation for the degree of Doctor of Philosophy.

Sheng S. Li, Chairman
Professor of Electrical Engineering

I certify that I have read this study and that in my opinion it conforms to acceptable standards of scholarly presentation and is fully adequate, in scope and quality, as a dissertation for the degree of Doctor of Philosophy.

David B. Tanner
Professor of Physics

I certify that I have read this study and that in my opinion it conforms to acceptable standards of scholarly presentation and is fully adequate, in scope and quality, as a dissertation for the degree of Doctor of Philosophy.

Gÿs Bosman
Professor of Electrical Engineering

I certify that I have read this study and that in my opinion it conforms to acceptable standards of scholarly presentation and is fully adequate, in scope and quality, as a dissertation for the degree of Doctor of Philosophy.

Robert M. Fox
Associate Professor of Electrical
Engineering

I certify that I have read this study and that in my opinion it conforms to acceptable standards of scholarly presentation and is fully adequate, in scope and quality, as a dissertation for the degree of Doctor of Philosophy.

Arnost Neugroschel
Professor of Electrical Engineering

This dissertation was submitted to the Graduate Faculty of the College of Engineering and to the Graduate School and was accepted as partial fulfillment of the requirements for the degree of Doctor of Philosophy.

August 1992

Winfred M. Phillips
Dean, College of Engineering

Madelyn M. Lockhart
Dean, Graduate School